

# Title

Estimating the glutamate transporter surface density in mouse hippocampal astrocytes

# Running title

Glutamate transporter expression in the mouse hippocampus

# Authors

Anca R. Rădulescu<sup>1</sup>, Cassandra L. Williams<sup>1</sup>, Gabrielle C. Todd<sup>2</sup>, Alex A. Lemus<sup>2</sup>, Haley E. Chesbro<sup>2</sup> and Annalisa Scimemi<sup>2\*</sup>

# \*Correspondence

scimemi@gmail.com (ORCID: 0000-0003-4975-093X)

# Institutional Affiliations

<sup>1</sup> Department of Mathematics, State University of New York at New Paltz

1 Hawk Drive, New Paltz, NY 12561, USA

<sup>2</sup> Department of Biology, State University of New York at Albany

1400 Washington Avenue, Albany, NY 12222, USA

# Acknowledgements

We would like to thank Pavel Ortinsky for comments on the manuscript, and Richard Leapman and Alioscka Sousa for help with 3D axial STEM tomography data collection. This work was supported by the Simons Foundation Collaboration Grants for Mathematicians (523763; A.R.), the SUNY New Paltz Research Scholarship and Creative Activities (A.R., C.L.W.), the SUNY Albany Research Foundation (A.S.), the National Institutes of Health (R03-NS102822; A.S.), and National Science Foundation (IOS1655365, IOS2011998; A.S.).

# Conflict of Interest Statement

The authors declare no competing financial interests.

# Data Sharing and Data Accessibility

The data included in this manuscript will be made available on Open Science Framework. The code for generating *in silico* astrocytes can be found at [https://github.com/scimemi/Astrocyte\\_generation](https://github.com/scimemi/Astrocyte_generation)

# Word Count

12,301

# Abstract

Glutamate transporters preserve the spatial specificity of synaptic transmission by limiting glutamate diffusion away from the synaptic cleft, and prevent excitotoxicity by keeping the extracellular concentration of glutamate at low nanomolar levels. Glutamate transporters are abundantly expressed in astrocytes. Previous estimates in the rat hippocampus suggest that the surface density of glutamate transporters in astrocytic membranes is  $\sim 10,800 \mu\text{m}^{-2}$ . Here, we estimate their surface density in astrocytic membranes of the mouse hippocampus, at different ages. By using realistic 3D Monte Carlo reaction-diffusion models, we show that varying the local glutamate transporter expression in astrocytes can alter profoundly the activation of extrasynaptic AMPA and NMDA receptors. Our findings show that the average density of astrocyte membranes and their surface density of glutamate transporters is higher in mice compared to rats, and increases with mouse age. There are stark differences in the density of expression of these molecules in different sub-cellular compartments, indicating that the extent to which astrocytes limit extrasynaptic glutamate diffusion depends not only on the level of astrocytic coverage, but also on the identity of the astrocyte compartment in contact with the synapse. Together, these findings provide information on the spatial distribution of glutamate transporters in the mouse hippocampus, which can be used in mathematical models of the spatiotemporal profile of extracellular glutamate after synaptic release.

# Keywords

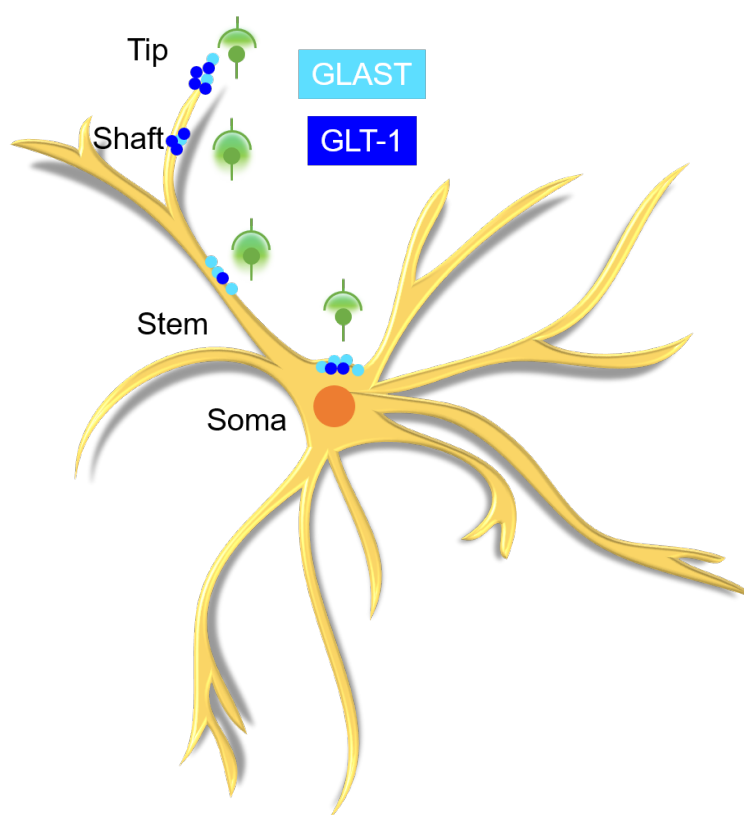
Astrocytes, Transmitter uptake, Glia and synaptic transmission, Modeling

# Table of Contents

## Main Points

- The astrocyte membrane density in the hippocampal neuropil is higher than in rats.
- The surface density of glutamate transporters in mouse astrocytes is higher than in rats and varies widely across different sub-cellular compartments.
- The identify of the astrocyte compartment in contact with a synapse, not only the extent of astrocytic coverage, is a main determinant of glutamate spillover and extrasynaptic receptor activation.

## Table of Contents Image



# Introduction

Glutamate is the main excitatory neurotransmitter released at chemical synapses in the brain. Small changes in the time course of glutamate clearance from the extracellular space can lead to pronounced changes in glutamate receptor activation, modulating synaptic efficacy throughout the brain. Glutamate removal from the extracellular space relies on passive diffusion and active transport, mediated by transporter molecules abundantly expressed in the plasma membrane of astrocytes [1–3]. In the rodent hippocampus,  $\sim 57\%$  of excitatory synapses are contacted by astrocytic membranes, which surround  $\sim 43\%$  of the synaptic perimeter [4].

Glutamate transport to the astrocyte cytoplasm is driven by the electrochemical gradient for  $\text{Na}^+$ ,  $\text{H}^+$  and  $\text{K}^+$  [5]. Under physiological conditions, one glutamate molecule is taken up from the extracellular space together with 3  $\text{Na}^+$  and 1  $\text{H}^+$  ions, while the counter-transport of 1  $\text{K}^+$  precedes the re-orientation of the transporter in the plasma membrane [5,6]. The unbalanced movement of charges associated with this stoichiometric current leads to the net influx of two positive charges for each transport cycle [7]. In addition, glutamate and  $\text{Na}^+$  binding to glutamate transporters opens a  $\text{Cl}^-$  conductance, which allows  $\text{Cl}^-$  to move across the membrane according to the direction of the driving force for  $\text{Cl}^-$  (i.e. the difference between the membrane potential and the reversal potential for  $\text{Cl}^-$ ) [8,9]. The current carried by  $\text{Cl}^-$  is referred to as the glutamate transport-coupled, non-stoichiometric anionic current [10]. It is not required for transport, but has been shown to control cell excitability and synaptic transmission for transporters expressed in neuronal presynaptic terminals [11]. There are five members in the glutamate transporter family and two of them, GLAST and GLT-1, are abundantly expressed in astrocytes [1]. GLAST and GLT-1 differ in their ratio of glutamate flux to anionic  $\text{Cl}^-$  current [7], pharmacological sensitivity [12], and developmental expression [13], but they share the same stoichiometry for glutamate transport, low transport efficiency ( $\sim 50\%$ ) and quaternary structure [14]. These transporters also show common and distinctive features for the regulation of their cell surface expression [15].

Our knowledge of the structure of eukaryotic glutamate transporters is largely based on the crystal structure of the outward-facing [16], inward-facing [17], open states [18],  $\text{Na}^+$ :substrate binding [19] and trimer assembly [20] of Glt<sub>Ph</sub>, a glutamate transporter homolog from the prokaryote *Pyrococcus horikoshii*. Glt<sub>Ph</sub> has  $\sim 37\%$  (high) amino acid identity with human GLT-1. For this reason, its structural features are currently thought to apply to other eukaryotic glutamate transporters, which have not yet been crystallized. The general consensus is that all glutamate transporters assemble as trimers, with each monomer functioning independently from the others [20]. The trimeric assembly delimits a bowl-shaped concave aqueous basin that prevents glutamate molecules unbinding from the transporters from being lost to extracellular diffusion [21] and contains molecular determinants that are involved in  $\text{Cl}^-$  channel activation of Glt<sub>Ph</sub> [18].

Structural, electrophysiological and modeling studies indicate that small changes in the density of expression of glutamate transporters can change profoundly the lifetime of glutamate in the extracellular space, receptor activation, and the time course of excitatory synaptic currents [22–24]. For this reason, there have been multiple attempts to determine the surface density of glutamate transporters in astrocytes and in small processes around synapses. The first estimates, based on electrophysiological studies in the hippocampus and cerebellum, suggested that glutamate transporters are at least two orders of magnitude more abundant than glutamate receptors, but the range of these estimates was very broad ( $1,315\text{--}13,150\ \mu\text{m}^{-2}$ ) [25–27]. An alternative approach, which we summarize here, relied on quantitative immunoblotting of protein extracts [28]. First, the immunoreactivity of GLAST and GLT-1 in whole tissue extracts was compared with the immunoreactivity of purified protein standards isolated with an immunoaffinity purification protocol which, in the adult rat hippocampus, led to density estimates of  $3,200\ \mu\text{m}^{-3}$  for GLAST and  $12,000\ \mu\text{m}^{-3}$

for GLT-1. *Second*, serial electron microscopy sections were used to identify astrocyte profiles and calculate the astrocyte membrane density ( $1.4 \mu\text{m}^2/\mu\text{m}^3$  in 7-8 week old rat hippocampus). *Third*, the astrocyte membrane density was used to convert the measure of glutamate transporter concentration into measures of glutamate transporter density in astrocytic membranes ( $2,300 \mu\text{m}^{-2}$  and  $8,500 \mu\text{m}^{-2}$  molecules for GLAST and GLT-1, respectively [28]). Therefore, the average surface density of all glutamate transporters in astrocytic membranes of the rat hippocampus was estimated to be  $\sim 10,800 \mu\text{m}^{-2}$  (i.e.  $\sim 3,600 \mu\text{m}^{-2}$  trimers). These values have been used extensively, particularly in computational models of glutamate clearance from the extracellular space not only in 7-8 week old rats, but for various ages and rodent species [23, 24, 29–36]. Whether this is a legitimate approach, and whether these estimates hold true for hippocampal astrocytes of mice of different ages remains unclear. Here we estimate the local surface density of GLAST and GLT-1 in different domains of the membrane of hippocampal astrocytes, in mice aged 2-3 weeks, 7-8 weeks and 15 months. By using *in silico* models, we show that the astrocyte tips, which contain the highest surface density of transporters, represent a small proportion of the entire astrocytic membrane, and estimate that most synapses are contacted by other compartments of the astrocyte membrane, with lower transporter expression.

# Methods

## Ethics statement

All experimental procedures were performed in accordance with protocols approved by the Institutional Animal Care and Use Committee at SUNY Albany and guidelines described in the National Institutes of Health's Guide for the Care and Use of Laboratory Animals.

## Mice

Unless otherwise stated, all mice were group housed and kept under 12 h:12 h light:dark conditions (lights on at 7 AM; lights off at 7 PM), with food and water available *ad libitum*. All experiments were performed on C57BL/6NCrl wild-type mice of either sex, aged from 14 postnatal days (P14) to 15 months.

## Dot blotting

Dot blot experiments were performed on protein extracts from the hippocampus of mice of either sex aged P14-21 (2-3 weeks), P53-55 (7-8 weeks), and 15 months. Membrane proteins were extracted using the Mem-PER Plus Membrane Protein Extraction Kit according to the manufacturer's instructions (Cat# 89842; ThermoFisher Scientific, Waltham, MA), using a mixture of protease and phosphatase inhibitors (10  $\mu$ l/ml, Cat# 78441; ThermoFisher Scientific, Waltham, MA). The total membrane protein concentration was determined using a Bradford assay (Cat# 5000006, BioRad, Hercules, CA). Purified, GST-tagged, recombinant protein of the human homologs of GLAST and GLT-1 (*Slc1a3*, Cat# H00006507-P02; *Slc1a2*, Cat# H00006506-P01; Abnova, Taipei, Taiwan) were serially diluted in phosphate buffered saline (PBS) and used to generate standard curves (**Figure 1**). Purified, recombinant protein and total hippocampal membrane protein were spotted on polyvinylidene difluoride (PVDF) membranes (Cat# P2563; MilliporeSigma, Burlington, MA). The membranes were blocked with 5% nonfat milk in Tris-buffered saline with 0.1% Tween 20 detergent (TBST) pH 7.6, and probed with primary antibodies (1 : 1,000 for GLAST and 1 : 500 for GLT-1) for 1-2 hours at room temperature in 5% bovine serum albumin (BSA) in TBST, pH 7.6. The blots were subsequently incubated with biotinylated horse anti-rabbit antibody (1 : 1,000) for 1 hour at room temperature in 5% BSA in TBST, pH 7.6. We amplified the immuno-labeling reactions using the Vectastain ABC kit (PK-6100, Vector Laboratories, Burlingame, CA) (1 : 2,000 for GLAST and 1 : 1,000 for GLT-1), and the Clarity Western enhanced chemiluminescence (ECL) system served as the substrate for the peroxidase enzyme (Cat# 1705060, Bio-Rad, Hercules, CA). A list of antibodies and reagents used for the dot blot experiments, together with their RRID, is reported in **Table 1**.

RRID	Item	Supplier
AB_955879	rabbit anti GLAST	Abcam, Cambridge, MA
AB_11005463	rabbit anti GLT-1	Novus, Littleton, CO
AB_2336201	biotinylated horse anti-rabbit	Vector Laboratories, Burlingame, CA
AB_2336819	Vectastain ABC kit	Vector Laboratories, Burlingame, CA

Table 1: **List of antibodies and reagents used for dot blot experiments.** The table lists the RRID number of antibodies and reagents used for dot blot analysis.

For our semi-quantitative analysis, protein dot intensities were collected as 16-bit images using a digital chemiluminescence imaging system using different exposure times (1s – 10min; c300, Azure Biosystems, Dublin, CA). Each image was converted to an 8-bit image for analysis using the Fiji

software (<https://fiji.sc/>). Only images collected at exposure times that did not lead to saturation were included in the analysis. The intensity of each dot was calculated as the raw integrated density (RID) in a region of interest (ROI) drawn around each dot. Background correction was carried out for each dot by subtracting the average RID of three dots containing only PBS. Each concentration of purified protein or total hippocampal membrane protein was spotted 2-3 times (1  $\mu$ l each). We averaged the RID values after background correction. Each age group contained protein samples from 3-6 mice. The molecular weights of the human, GST-tagged, recombinant proteins (87,387 Da and 89,988 Da for GLAST and GLT-1, respectively) and of the endogenous mouse proteins (59,619 Da and 62,027 Da for GLAST and GLT-1, respectively) were calculated based on their amino acid sequences using the software BioEdit (<https://bioedit.software.informer.com/7.2/>). Mass corrected standard curves correlating average RID in each ROI to the amount of purified GLAST or GLT-1 spotted onto the membrane were fitted using the following sigmoidal curve (**Figure 1**):

$$F(x) = \frac{max}{1 + \exp\left(\frac{x_{half} - x}{rate}\right)} \quad (1)$$

Based on this fit, we calculated the fraction of GLAST and GLT-1 in dots from total hippocampal membrane proteins. We assumed that there are 97.8 g/Kg of brain tissue [28], the density of brain tissue is 1.05  $gcm^3$  [28], and calculated the surface density of astrocytic membrane in *stratum radiatum* of the mouse hippocampus using 3D axial STEM tomography reconstructions (see below). Based on this analysis, the estimated astroglial surface density is 3.15  $\mu m^2/\mu m^3$ . With these assumptions, we were able to estimate the average number of GLAST and GLT-1 molecules/ $\mu m^2$  on the membrane surface of hippocampal astrocytes in tissue samples from three age groups: 2-3 week, 7-8 week and 15 month old mice.

## Electron microscopy and axial STEM tomography

Acute hippocampal slices processed for electron microscopy analysis were prepared as described for the electrophysiology experiments, from P17 mice. Slices were microwave-fixed for 13 s in 6% glutaraldehyde, 2% PFA, 2 mM  $CaCl_2$  in 0.1 N sodium cacodylate buffer and stored overnight at 4°C. After three washes in 0.1 N cacodylate buffer, we cut samples from the middle part of CA1 *stratum radiatum*,  $\sim 100 \mu m$  away from the pyramidal cell layer. These samples were treated with 1% osmium tetroxide for 1 hour on ice, en bloc mordanted with 0.25% uranyl acetate at 4°C overnight, washed and dehydrated with a graded series of ethanol, and embedded in epoxy resins. Thin sections (70-90 nm) were counter-stained with lead citrate and uranyl acetate and examined on a JEOL 1200 EX transmission electron microscope. Images were collected with a CCD digital camera system (XR-100, AMT, Woburn, MA). To visualize the arrangement of post-synaptic densities (PSDs) and astrocytic processes, thick sections ( $\sim 1 - 1.5 \mu m$ ) were cut from regions of CA1 *stratum radiatum* and electron tomograms were collected in a 300 kV electron microscope operated in the scanning transmission electron microscopy (STEM) mode, as described previously [37,38]. A sample thickness of 1  $\mu m$  (enabled by axial STEM tomography) provided sufficient sample depth to visualize features of interest in their entirety, such as synapses. In contrast to STEM tomography, conventional TEM tomography is limited to a specimen thickness of  $\sim 400$  nm and cannot be applied to such thick sections because the transmitted electrons undergo multiple inelastic scattering processes, resulting in images that are blurred by chromatic aberration of the objective lens. Axial STEM tomography is not affected by chromatic aberration because the objective lens that forms the electron probe is in front of the specimen. Dual-axis tilt series of selected sections were recorded using an FEI Tecnai TF30 TEM/STEM operating at 300 kV (1.5° tilt increment, tilt range from 55° to -55°, pixel size = 5.6 nm). Image registration, tomogram generation, tracing, surface area and volume measures were performed using IMOD 4.7 (<https://bio3d.colorado.edu/imod/>). In



the tomograms, we identified astrocytic processes based on their lack of synaptic vesicles and post-synaptic densities and because they did not give rise to pre- or post-synaptic terminals. Orthoslices through the STEM tomograms showed that astrocytic processes contained glycogen granules, intermediate filament bundles and a more electron-lucent cytoplasm with respect to that of neurons. The astrocytic processes were traced for the entire thickness of the reconstructed volume (1.5  $\mu\text{m}$ ). We reconstructed all astrocytic processes in a tissue block.

## Acute slice preparation

Acute coronal slices of the mouse hippocampus were obtained from C57BL/6NCrl mice of either sex (P16–21), deeply anesthetized with isoflurane and decapitated in accordance with SUNY Albany Animal Care and Use Committee guidelines. The brain was rapidly removed and placed in ice-cold slicing solution bubbled with 95% O<sub>2</sub>/5% CO<sub>2</sub> containing the following (in mM): 119 NaCl, 2.5 KCl, 0.5 CaCl<sub>2</sub>, 1.3 MgSO<sub>4</sub> · H<sub>2</sub>O, 4 MgCl<sub>2</sub>, 26.2 NaHCO<sub>3</sub>, 1 NaH<sub>2</sub>PO<sub>4</sub>, and 22 glucose, 320 mOsm, pH 7.4. The slices (250  $\mu\text{m}$  thick) were prepared using a vibrating blade microtome (VT1200S; Leica Microsystems, Buffalo Grove, IL). Once prepared, the slices were stored in slicing solution in a submersion chamber at 36°C for 30 min and at room temperature for at least 30 min and up to 5 hours. Unless otherwise stated, the recording solution contained the following (in mM): 119 NaCl, 2.5 KCl, 2.5 CaCl<sub>2</sub>, 1 MgCl<sub>2</sub>, 26.2 NaHCO<sub>3</sub>, and 1 NaH<sub>2</sub>PO<sub>4</sub>, 22 glucose, 300 mOsm, pH 7.4. We identified the hippocampus under bright field illumination and astrocytes using differential interference contrast, using an upright fixed-stage microscope (BX51 WI; Olympus Corporation, Center Valley, PA). Whole-cell, voltage-clamp patch-clamp recordings were made using patch pipettes containing (in mM): 120 CsCH<sub>3</sub>SO<sub>3</sub>, 10 EGTA, 20 HEPES, 2 MgATP, 0.2 NaGTP, 5 QX-314Br, 290 mOsm, pH 7.2. Biocytin 0.2-0.4% was added to the internal solution. All recordings were obtained using a Multiclamp 700B amplifier (Molecular Devices, San Jose, CA), filtered at 10 KHz, converted with an 18-bit 200 KHz A/D board (HEKA Instrument, Holliston, MA), digitized at 10 KHz, and analyzed offline with custom-made software (A.S.) written in IgorPro 6.37 (Wavemetrics, Lake Oswego, OR). Patch electrodes (#0010 glass; Harvard Apparatus, Holliston, MA) had tip resistances of  $\sim 5\text{ M}\Omega$ . Series resistance ( $\sim 20\text{ M}\Omega$ ) was not compensated, but was continuously monitored and experiments were discarded if this changed by more than 20%. All reagents were purchased from Millipore Sigma (Burlington, MA). All recordings were performed at room temperature.

## Biocytin fills, proExM and 2P-LSM image acquisition

Patched astrocytes were maintained in the whole-cell configuration at a holding potential of -90 mV for at least 30 min to allow biocytin to fill small cellular compartments. At the end of this time, the patch pipette was gently removed and the slice was fixed with PBS 4% PFA overnight at 4°C, cryoprotected in PBS 30% sucrose and stored in PBS for up to 1 week. Each slice was then incubated in 0.1% streptavidin-Alexa Fluor 488 conjugate and 0.1% Triton X-100 for 3 hours at room temperature. The day before starting the protein retention expansion microscopy (proExM) protocol [39], we incubated the slice with DAPI Fluoromount G overnight at 4°C (Cat# 0100-20; SouthernBiotech, Birmingham, AL) to ensure the whole slice could be visualized under fluorescence microscopy to localize the biocytin-filled, streptavidin-labelled astrocyte. The proExM protocol, originally developed by [39], was analogous to the one used in our previous work [40]. Briefly, each slice was incubated with 200  $\mu\text{l}$  of anchoring solution overnight at room temperature. The following day, the slices were gelled and digested with Proteinase K overnight at room temperature. Subsequently, they were expanded using three consecutive incubations with distilled water for 15 min each. The expanded gels containing biocytin-filled astrocytes were then covered with 2% agarose and submerged in distilled water before being imaged with a custom-made two-photon



laser-scanning microscope. The two-photon laser scanning system (Scientifica, Clarksburg, NJ) was powered by a Ti:sapphire pulsed laser (Coherent, Santa Clara, CA) tuned to 760 nm and connected to an upright microscope with a 60 $\times$ /1.0 NA objective (Olympus Corporation, Center Valley, PA). The green fluorescent signal was separated from the red using a 565 nm dichroic mirror and filtered using FITC filter sets (Olympus Corporation, Center Valley, PA). We averaged eight frames for each optical section (260 $\times$ 260  $\mu$ m, 512 $\times$ 512 pixels, pixel size: 0.51  $\mu$ m) and collected z-stacks for a total distance of  $\sim$ 200  $\mu$ m (in 1.2  $\mu$ m steps). The composition of the anchoring, gelling and digestion solution are reported in **Table 2**. Note that the linear expansion factor of proExM was  $\sim$ 2.

<b>Anchoring solution (200 <math>\mu</math>l/slice)</b>	<b>Cat#</b>	<b>Supplier</b>	<b>Amount</b>
Acryloyl X, SE	A20770	Life Technologies	0.1 mg/ml
DMSO	472301	Millipore Sigma	2 $\mu$ l
PBS	P4417	Millipore Sigma	198 $\mu$ l

<b>Monomer solution (188 <math>\mu</math>l/slice)</b>	<b>Cat#</b>	<b>Supplier</b>	<b>Amount</b>
Sodium acrylate	408220	Millipore Sigma	86 mg/ml
Acrylamide	A9099	Millipore Sigma	25 mg/ml
N,N'-methylenebisacrylamide	M7279	Millipore Sigma	1.5 mg/ml
NaCl	215700	BeanTwon Chemical	117 mg/ml
PBS 10X	P4417	Millipore Sigma	18.8 $\mu$ l (1:10)
Distilled water			169.2 $\mu$ l

<b>Gelling solution (200 <math>\mu</math>l/slice)</b>	<b>Cat#</b>	<b>Supplier</b>	<b>Amount</b>
Monomer solution			188 $\mu$ l
4-hydroxy-TEMPO	176141	Millipore Sigma	4 $\mu$ l (0.01%)
TEMED	T9281	Millipore Sigma	4 $\mu$ l (0.2% w/w)
APS	A3678	Millipore Sigma	4 $\mu$ l (0.2% w/w)

<b>Digestion solution (200 <math>\mu</math>l/slice)</b>	<b>Cat#</b>	<b>Supplier</b>	<b>Amount</b>
Tris pH 8.0	AM9855G	Ambion	50 mM
EDTA	03690	Fluka Analytical	1 mM
Triton X-100	X100	Millipore Sigma	0.5% v/v
Guanidine hydrochloride	G3272	Millipore Sigma	0.8 M
Proteinase K	P6556	Millipore Sigma	8 U/ml

Table 2: **Composition of anchoring, gelling and digestion solution for proExM.** The tables list the chemical reagents that were used to process hippocampal slices for proExM.

## Analysis of 2P-LSM images of proExM treated tissue

Adjacent z-stack tiles acquired using 2P-LSM were stitched using the Pairwise Stitching plugin available in Fiji (<https://imagej.net/Fiji>), with Linear Blending Fusion Method (check peaks value: 95). After stitching, we imported the z-stacks into Bitplane Imaris 9.3.1 (Oxford Instruments,

Abingdon, UK) and converted them to 8-bit .ims files. The next steps aimed to isolate the biocytin-filled astrocyte 4 from other gap-junction coupled astrocytes, typically much dimmer. *First*, we smoothed each image using a Gaussian filter with a width of  $0.51\ \mu\text{m}$ , matching the  $x,y$  pixel size of the image stacks collected using 2P-LSM. *Second*, we generated a surface mask using an absolute intensity threshold that allowed us to get rid of all voxels with an intensity value greater than 20. *Third*, we segmented the surface mask using a seeded region-growing method using a seed point diameter of  $20\ \mu\text{m}$  and a quality threshold of 10. *Fourth*, we manually deleted surfaces outside the patched astrocyte. This allowed us to refine the surface mask to be used in the next step. *Fifth*, we applied this refined surface mask to the original z-stack. This allowed us to isolate voxels belonging to the astrocyte of interest based on their location (i.e. they resided within the mask) and gray intensity (i.e. gray intensity  $>1$ ). All other voxels outside this mask were assigned an intensity value of zero. To generate the cytoplasmic volume of the astrocyte, in Bitplane Imaris, we selected the channel created using a gray intensity  $>1$ , applied the seeded region growing algorithm (seed point diameter:  $20\ \mu\text{m}$ ) and manually set an arbitrary quality threshold that allowed us to identify only one surface within the astrocyte (typically between 10 and 20). No surface smoothing was applied. To complete the surface rendering, Bitplane Imaris uses a marching cubes computer graphics algorithm. Briefly, the marching cubes algorithm allows to determine whether an arbitrary set of points is within the boundary of an object. To do this, the volume occupied by these points is divided into an arbitrary number of cubes and the algorithm tests whether the corners of those cubes lie within the selected object. All cubes where corners are found both within and outside of the object produce a set of points that define the boundary of a surface that identifies the cytoplasmic volume [41]. We used a similar approach to generate the bounding volume. In this case, we applied a surface smoothing factor of  $5\ \mu\text{m}$ , meaning that structural details smaller than  $5\ \mu\text{m}$  ( $2.5\ \mu\text{m}$  without proExM) were lost. To generate filaments, which represent astrocyte branches of different levels, we selected the masked channel containing only the biocytin-filled astrocyte, and used the Autopath (no loops) filament tracing algorithm for big data sets. The Autopath (no loops) algorithm produces a tree-like filament (based on local intensity contrast) that connects large ( $25.4\ \mu\text{m}$  at the soma) to small seed points ( $1\ \mu\text{m}$  at the most distal processes). The origin of the primary branches was set to the center of the soma. For the filament branch count, we masked the portion of the primary branches that fell within the radius of the soma. We calculated branch diameters from input parameters rather than from the image intensity values.

### 3D Monte Carlo reaction-diffusion simulations

The geometry of seven adjacent synaptic contacts was created *in silico* with an open source program (Blender 2.79b) and an add-on that allows creating computational models for use in a Monte Carlo simulation environment (MCell) and visualizing the simulation results (CellBlender 3.5.1.1). The simulations were run within a cube (world), with absorptive properties for all diffusing molecules ( $3\ \mu\text{m} \times 3\ \mu\text{m} \times 3\ \mu\text{m}$ ). Each pre- and post-synaptic terminal was modelled as a hemisphere with radius  $0.25\ \mu\text{m}$ , positioned either at the center of the world or  $1\ \mu\text{m}$  away (center-to-center) along the vertices of a hexagonal polygon centered at the origin of the world (i.e. the edge-to-edge distance was  $500\ \text{nm}$  for consistency with [22]). The two hemispheres were separated from each other by a  $20\ \text{nm}$  high synaptic cleft. Four synapses (i.e.  $4/7 = 57\%$ ) had  $43\%$  of their synaptic perimeter flanked by a  $50\ \text{nm}$  thick,  $250\ \text{nm}$  tall portion of an astrocyte, which we represented as a section of a cylindrical sheet located  $20\ \text{nm}$  away from the edge of the synapse. This organization is consistent with previous electron microscopy analysis of rodent hippocampal synapses [4, 22]. We varied the density of the glutamate transporters expressed in the astrocytic processes within the range  $100\text{-}10,000\ \mu\text{m}^{-2}$ , as shown in **Figure 3**. We used this model to estimate the glutamate concentration profile at all synapses. The glutamate transporters were modeled using a simplified kinetic scheme [24] (**Figure 3B**). All rates were adjusted for  $Q_{10} = 3$ ,

to approximate the transporter kinetics at 35°C. At  $t = 0$ , 2,000 glutamate molecules were released from a point source placed at the origin of the world, at the center of the synaptic cleft of the central synapse. Glutamate diffused away with a diffusion coefficient  $D^* = 3.30e^{-6}$  cm<sup>2</sup>/s within the synaptic cleft [42]. Outside the cleft the apparent diffusion coefficient was set to  $D^* = 1.29e^{-6}$  cm<sup>2</sup>/s, to account for a tortuosity value of  $\lambda = 1.6$  [24]. Each simulation consisted of 100,000 iterations with a time step  $t = 1$   $\mu$ s (therefore spanning a 100 ms time window), and was repeated 100 times. Glutamate was removed from the simulation environment once it hit the inner surface of the world, surrounding all synapses (i.e. the surface of the world was absorptive for glutamate). Glutamate hitting the surfaces of all other objects bounced back in the extracellular space (i.e. the surface of all other geometries in the simulation was reflective for glutamate). The glutamate concentration was monitored every  $t = 10$   $\mu$ s. We used these simulations to calculate the glutamate concentration in and out of the synaptic cleft, as shown in **Figure 3C,D**. These waveforms were imported into ChanneLab 2.041213 (Synaptosoft) and used to calculate the open probability of synaptic and extra-synaptic AMPA and NMDA receptors (**Figure 3E,F**). The kinetic rates for AMPA receptors were set in accordance to [43]. The kinetic rates for NMDA receptors were set in accordance to [44]. In both cases, the reaction rates were adjusted by  $Q_{10} = 3$ , to approximate the receptor and transporter kinetics at 35°C.

## Generation of a 3D model of astrocytes

Our *in silico* rendition of astrocytes was based off our morphological analysis of biocytin-filled astrocytes processed with proExM and imaged with 2P-LSM, following conversion for a linear expansion factor of 2 [40]. Each model astrocyte consisted of a spherical soma and a tree of processes that branched off of it. The main features of reconstructed and model astrocytes are summarized in **Table 3**.

The astrocyte branching tree was created recursively from a set of primary branches emerging from the soma. The model was developed using custom-made routines written in MATLAB2019 (Mathworks, Natick, MA). The recursive branching mechanism was based on the principle that new branches, with higher branching level, can be formed by each existing branch, as shown in **Figure 4**. The branching algorithm allowed us to control the number of branch levels, their length and diameter, and allowed for cell-to-cell branch variability. The algorithm incorporates a number of experimentally-derived constraints and features, which are described below.

**Astrocyte branch generation.** The number of primary branches departing from the soma was chosen randomly between 3 – 7 for each model astrocyte, consistent with the number of primary branches measured through the morphological analysis of biocytin-filled astrocytes (**Table 3**). The primary branches emerged at random locations from the soma, and extended radially along straight lines. Each primary branch could generate up to  $M = 15$  daughter (secondary) branches in a 3D space (at intervals that will be described below). The opening angles of the daughter branches, calculated with respect to the direction of the primary branch, were all set to  $\pi/6$ , and their rotation angles were chosen randomly within the range from  $0 - 2\pi$ . The operation was then repeated recursively for up to  $N = 11$  branching levels, consistent with the maximum number of branching levels detected experimentally (**Figure 4E**). At each branching point, each parent branch could either generate a daughter branch and continue on, or terminate (see termination criteria below). The angle between the direction of the daughter branch and that of the parent branch increased from  $\pi/6$  (as established for the secondary branches) by  $\pi/80$  at each branching level. This was a simple linear model that best approximated the increasing trend in the size of the branching angles at each branching level, as observed in the reconstructed astrocytes (see **Figure 4H**). The segments connecting any two branching points were approximated as cylinders. An exception was made for the tips of the astrocyte terminal processes, which were modeled as

Var	Description	Experiments			Model		
		mn ( $\mu\text{m}$ )	SD	n	mn ( $\mu\text{m}$ )	SD	n
$r_{soma}$	soma radius	4.9	1.1	12	5	0	1
$R_{astro}$	cell radius	120.7	31.5	10	97.8	28.9	10
$n_I$	num. branch I	4.5	1.9	12	5.4	0.4	10
$\chi_0$	dist. soma – bpt 1 (I)	6.5	4.1	41	5.1	2.8	54
$\chi_1$	dist. bpt 1 – 2 (I)	4.9	17.5	28	5.3	3.0	54
$\chi_2$	dist. bpt 2 – 3 (I)	4.6	18.4	20	5.1	2.9	54
$\chi_3$	dist. bpt 3 – 4 (I)	3.2	8.2	12	5.2	2.8	54
$\chi_4$	dist. bpt 4 – 5 (I)	3.4	6.6	9	5.2	2.9	54
$\chi_5$	dist. bpt 5 – 6 (I)	2.1	1.6	2	5.3	2.9	54
$\chi_6$	dist. bpt 6 – 7 (I)	1.1	0.3	2	5.3	2.8	54
$\chi_7$	dist. bpt 7 – 8 (I)	3.6	0.0	1	5.1	2.7	51
$\chi_8$	dist. bpt 8 – 9 (I)	-	-	-	5.5	3.2	41
$\chi_9$	dist. bpt 9 – 10 (I)	-	-	-	5.5	3.2	31
$\lambda_0$	dist. base - bpt 1 (II)	4.3	0.7	41	5.2	2.8	559
$ratio_{x,y}$	$x,y$ asymmetry ratio	2.1	0.3	12	-	-	-
$\delta_n$	tip diameter	0.15 (0.02-0.24)	0.02	73	0.08* (0.02-0.26)	-	21,726

Table 3: **List of parameters describing astrocyte morphology *in vitro* and *in silico*.** Morphological measures were determined experimentally and used to implement the model representation of astrocytes. Abbreviations: number of primary branches (num. branch I), distance (dist.), branching point (bpt), primary branch (I), secondary branch (II).

hemispheres. The geometry of the tips and its consequences are further discussed in a separate section of this manuscript.

**Astrocyte branch length generation.** We generated the astrocyte branch segments (i.e. the portion of a branch between two consecutive branching points) in a way that would best fit our average empirical measures, while also accounting for the existence of cell-to-cell, in-cell and branch-to-branch variability. For each astrocyte, we first generated a random value  $c_0$  within the range  $0 - 15 \mu\text{m}$ , to be used as a cell-wide baseline for segment lengths. In order to allow variability between primary branches (which exists in real astrocytes) we customized a specific segment length baseline for each primary branch, by randomly choosing a specific value of  $c \leq c_0$ . All segments within the tree generated by a primary branch (i.e. the segments along the primary branch and all its daughter branches) were generated by adding a random term  $\leq 5 \mu\text{m}$  to the baseline value  $c$ . This modeling scheme allowed us to best fit a collection of experimentally-derived measurements: the branch segments length ( $\chi_0 - \chi_9$  and  $\lambda_0$ ), the average branch length for each branching level, and the Sholl profile of the astrocytes (**Figure 4**).

**Astrocyte branch diameter generation.** The diameter of the cylinders representing the primary branches was set to  $5 \mu\text{m}$ . To establish a rule to determine the diameter of the daughter branches, we considered previous attempts to solve this problem in neurons. In neurons, the input conductance of dendritic branches depends on the  $3/2$  power of the branch diameter [45]. When the constraint that the sum of the  $3/2$  power values of the daughter branch diameter is equal to the  $3/2$  power of the parent branch diameter, the entire dendritic tree of the neuron can be mapped to an equivalent cylinder (provided also that all terminal branches end at the same electrotonic distance

from the trunk). This rule is commonly referred to as the 3/2 rule [46,47]. We asked whether this rule also applied to astrocytes. To do this, we measured the average diameter of the primary ( $\delta_1 = 1.3 \pm 0.7 \mu\text{m}$  (n=46)) and secondary branches ( $\delta_2 = 0.8 \pm 0.3 \mu\text{m}$  (n=76)) in a group of 10 astrocytes. We then calculated the values of  $\delta_2$  that could be obtained once we set  $\delta_1 = 1.3 \pm 0.7 \mu\text{m}$ , using various values for  $k$  in the relationship  $D^{k/2} = d_1^{k/2} + d_2^{k/2}$ , where  $d_1 = d_2$ . The most accurate prediction of the experimental data (i.e.  $\delta_2 = 0.8 \pm 0.3 \mu\text{m}$ ) was obtained using the 3/2 rule. This findings suggested that the 3/2 rule holds true for both neurons and astrocytes. Based on this information, when creating daughter branches in our model, we determined the diameter  $d_1$  of the parent branch after the branching point and the diameter  $d_2$  of the daughter branch based on the diameter  $D$  of the parent branch before the branching point, based on the 3/2 rule:  $D^{3/2} = d_1^{3/2} + d_2^{3/2}$  [45–47]. To account for variability in the size of emerging branches, we set  $d_1 = (f \cdot d_2)$ , and used the 3/2 rule in the form:  $D^{3/2} = (f \cdot d_2)^{3/2} + d_2^{3/2}$ . Here,  $d_2$  is the diameter of the daughter branch, and  $(f \cdot d_2)$  is the diameter of the parent branch after the branching point. In our simulations,  $f$  was chosen randomly within the interval 1 – 1.5.

**Astrocyte branch termination conditions.** While all astrocytes were allowed to have up to  $M = 15$  branching points along each primary branch, and up to  $N = 11$  branching points in each higher order branches, our algorithm also allowed us to terminate a branch at any branching point, based on their diameter. In each model astrocyte, a maximum diameter  $d_{\text{max}}$  was generated randomly for each primary branch within the interval 0.02-0.15  $\mu\text{m}$  (the range was established based on the 3D axial STEM tomography analysis of astrocytic processes [48]). The generation of daughter branches along a parent branch was terminated if the diameter of any of the two emerging branch segments (as computed according to the 3/2 rule described above) was lower than  $d_{\text{max}}$ . The resulting range for tip diameters in model astrocytes was similar to that obtained from biocytin-filled astrocytes (Table 3).

**Morphology analysis of model astrocytes.** Each *in silico* generated astrocyte was designed to incorporate fixed terms (i.e. the somatic radius, the diameter of the primary branches, the maximum number of branch levels and the opening angle for each level) and random terms (i.e. branch length, diameter ratios are branch points, terminal diameter). This allowed our 3D models to produce a large variety of astrocyte sizes and shapes (Figure 4B), consistent with experimental data. For each model astrocyte, we computed the cytoplasmic volume and total branch surface area, total branch length, average segment length  $\lambda$  and  $\chi$ , average tip diameter, number of branches per level and average branch length per level. For each astrocyte, we computed the 3D Sholl profile, using 0.5  $\mu\text{m}$  spaced spherical shells. In Figure 4G, we illustrate these 3D Sholl profiles of 10 randomly generated astrocytes, as well as their average, which agrees with the experimentally derived 3D Sholl profiles.

## Glutamate transporter spatial distribution

We calculated the maximum number of transporters that could be placed in each model astrocyte, and the fraction of the membrane surface area they occupied. Our estimates were based off the crystal structure of glutamate transporter trimers of the prokaryotic homolog *Glt<sub>Ph</sub>*, which can be approximated to a prism with triangular base of 8 nm side length and 6.5 nm height (see Figure 5)A,B [16]. We first considered how the geometry of these prisms can optimally fit that of a circle, a sphere (approximating the shape of the astrocyte soma) and a cylinder (approximating the shape of each astrocyte branch segment). The optimization constraints stemmed from the curvature of the membrane surface, which introduced some room between adjacent trimers, to avoid collision of the portions of these trimers protruding into the astrocyte cytoplasm or in the



extracellular space (depending on the concavity/complexity of the branching points). Our optimal distribution was based on trimers fitting into spheres or cylinders that abide by this constraint, and maximize the space available on the membrane surface. While the theoretical trimer distribution that we propose is not always possible precisely in the form described (due to geometric limitations), our formulas can nonetheless be used as general close estimates, especially for the some/branch radius ranges in which the model operates. Each trimer replaces a curved portion of a sphere or cylinder. We computed analytically the area of this portion, as a function of the (sphere/cylinder) radius and of the trimer size. Last, we used these estimates to calculate the maximum surface density and surface area occupied by these molecules over the entire astrocyte, taking into account the potential effects introduced by angle constraints and transporter crowding around branching points. Our measurements took into account changes in the protrusion of transporters in the astrocyte cytoplasm, due to transporters moving across different conformational states.

**Distributing trimers on the surface of a sphere.** To estimate the maximum number of transporter trimers that can be placed on the surface of a sphere of radius  $r_1$ , we computed the maximum triangular trimer bases that can cover, without colliding, a smaller sphere of radius  $r_{-1}$  (accounting for the depth of cytoplasmic protrusion of the transporters  $r_1 - r_{-1}$ ). We did this using the geometry of lunar triangles. A spherical lune is defined as the surface that lies between two great circles that intersect each other on the surface of a sphere (**Figure 5C**). In our case, for a fixed triangle in the  $w$ -triangulation, one can consider the three planes defined by each pair of adjacent vertices, together with the center of the sphere. Each plane defines a great circle on the sphere, and each pair of great circles delimits a lune. We considered the spherical “lunar” triangle at the intersection of these three lunes with identical areas  $A_{lune} = 4\alpha r_{-1}^2$ , where  $\alpha$  is the angle between the great circles defining the lune (in this case, identical for all three lunes). Notice that, for a  $w$ -triangulation of the sphere, the entire spherical surface can be written as a union of all lunar triangles defined by the triangulation, leading to Equation 24. The area  $A^{\Delta_s}$  of the “lunar” triangle can be calculated using Girard’s Theorem by expressing the area of the sphere as illustrated in **Figure 7A**:

$$4\pi r_{-1}^2 = 3A_{lune} - 4A^{\Delta_s}$$

This gives us an expression for the area of the lunar equilateral triangle in terms of the sphere radius and the lunar angle.

$$A^{\Delta_s} = r_{-1}^2(3\alpha - \pi) \quad (2)$$

The angle  $\alpha$  was computed using trigonometry in the spherical triangle (in **Figure 7A**, call  $\gamma = a = b = c$  the small arc defined by each of the triangle vertices on the corresponding great circle, and use the identity:  $\cos a = \cos b \cos c + \sin b \sin c \cos \alpha$ ):

$$\cos \alpha = \frac{\tan(\gamma/2)}{\tan \gamma} = \frac{1 - \tan^2(\gamma/2)}{2} \quad (3)$$

Since  $\sin\left(\frac{\gamma}{2}\right) = \frac{\omega}{2r_{-1}}$ , the area of the lunar triangle corresponding to an  $w$ -triangulation of a sphere of radius  $r_{-1}$  is:

$$A^{\Delta_s} = r_{-1}^2(3\alpha - \pi) = r_{-1}^2 \left[ 3 \arccos \left( \frac{2r_{-1}^2 - \omega^2}{4r_{-1}^2 - \omega^2} \right) - \pi \right] \quad (4)$$

**Computation of the sphere surface area occupied by transporters.** The triangular base of a glutamate transporter trimer can be viewed in a reference  $(x, y)$  coordinate plane as an equilateral triangle of side  $\omega$  centered at the origin, as shown in **Figure 5F**. We calculated the surface area  $A_{sphere}^{\Delta}$  of the portion of the sphere of radius  $r_1$  situated above this triangle. This represents

the portion of the astrocyte surface area occupied by a transporter trimer of side length  $w$ . The computation of the integral was carried out in polar coordinates, for convenience:

$$\begin{aligned} \frac{A_{sphere}^{\Delta}}{3} &= \iint_D \sqrt{\left(\frac{\partial z}{\partial x}\right)^2 + \left(\frac{\partial z}{\partial y}\right)^2 + 1} dA = \iint_D \frac{r_1}{\sqrt{r_1^2 - x^2 - y^2}} dA \\ &= \int_{\theta=-\pi/6}^{\theta=\pi/2} \int_{r=0}^{r=\frac{\omega}{2\sqrt{3}\sin(\theta+\pi/3)}} \frac{r_1}{\sqrt{r_1^2 - r^2}} r dr d\theta \\ &= r_1^2 \int_{\theta=-\pi/6}^{\theta=\pi/2} 1 - \sqrt{1 - \frac{\omega^2}{12r_1^2 \sin^2(\theta + \pi/3)}} d\theta \end{aligned}$$

With the substitution  $\tau = \theta + \pi/3$  and with the notation  $\alpha = \frac{\omega}{2\sqrt{3}r_0}$ , we obtained:

$$A_{sphere}^{\Delta} = 3r_1^2 \int_{\tau=\pi/6}^{\tau=5\pi/6} 1 - \sqrt{1 - \frac{\alpha^2}{\sin^2(\tau)}} d\tau \quad (5)$$

To derive an explicit dependence of  $A_{sphere}^{\Delta}$  on parameters, we solved the remaining integral with the help of Integral Calculator (<https://www.integral-calculator.com>, accessed March 17, 2019):

$$\begin{aligned} F(\tau) &= \int \sqrt{1 - \frac{\alpha^2}{\sin^2(\tau)}} d\tau \\ &= \alpha \sin^{-1} \left( \frac{\alpha \cot \tau}{\sqrt{1 - \alpha^2}} \right) - \tan^{-1} \left( \frac{\cos \tau}{\sqrt{\sin^2 \tau - \alpha^2}} \right) \end{aligned} \quad (6)$$

where  $\alpha$  can be considered small enough so that  $\alpha^2 < 1/2$  (which implies  $\sin^2 \tau - \alpha^2 > 0$ , since  $\pi/6 \leq \tau \leq 5\pi/6$ ). The definite integral can then be calculated as:

$$\begin{aligned} \int_{\pi/6}^{5\pi/6} \sqrt{1 - \frac{\alpha^2}{\sin^2(\tau)}} d\tau &= F(5\pi/6) - F(\pi/6) = \\ &= 2 \tan^{-1} \left( \frac{\sqrt{3}}{\sqrt{1 - 4\alpha^2}} \right) - 2\alpha \sin^{-1} \left( \frac{\sqrt{3}\alpha}{\sqrt{1 - \alpha^2}} \right) \\ &= 2 \tan^{-1} \left( \frac{3r_1}{\sqrt{3r_1^2 - \omega^2}} \right) - \frac{\omega}{\sqrt{3}r_1} \sin^{-1} \left( \frac{\sqrt{3}\omega}{12r_1^2 - \omega^2} \right) \end{aligned} \quad (7)$$

In conclusion:

$$A_{sphere}^{\Delta} = 2\pi r_1^2 - 3r_1^2 \left[ 2 \tan^{-1} \left( \frac{3r_1}{\sqrt{3r_1^2 - \omega^2}} \right) - \frac{\omega}{\sqrt{3}r_1} \sin^{-1} \left( \frac{\sqrt{3}\omega}{12r_1^2 - \omega^2} \right) \right] \quad (8)$$

**Computation of the cylinder surface area occupied by transporters.** We called  $A_{cyl}^{\Delta}(r_{cyl})$  the area that each trimer occupies on the surface of a cylinder of radius  $r_{cyl}$ . As illustrated in **Figure 8A**, this can be calculated as the area of the cylindrical region lying on top of the domain  $D$ , enclosed by an equilateral triangle of side  $\omega$  centered at the origin. Since the cylinder of radius



$R$  is given by the equation  $z = \sqrt{r_{cyl}^2 - x^2}$ , the area of the cylinder  $A(R)$  above the triangle can be expressed as the double iterated integral:

$$\begin{aligned} A_{cyl}^{\Delta}(r_{cyl}) &= \iint_D \sqrt{\left(\frac{\partial z}{\partial x}\right)^2 + \left(\frac{\partial z}{\partial y}\right)^2 + 1} dA = 2 \int_0^{\omega/2} \int_{-\omega/2\sqrt{3}}^{\omega/\sqrt{3}-\sqrt{3}x} \frac{r_{cyl}}{\sqrt{r_{cyl}^2 - x^2}} dy dx \\ &= \sqrt{3}\omega r_{cyl} \sin^{-1}\left(\frac{\omega}{2r_{cyl}}\right) + \sqrt{3}r_{cyl} \sqrt{4r_{cyl}^2 - \omega^2} - 2\sqrt{3}r_{cyl}^2 \end{aligned} \quad (9)$$

# Results

## Quantification of glutamate transporter variants in mouse hippocampal astrocytes

We quantified GLAST and GLT-1 protein levels in membrane protein extracts of the mouse hippocampus using dot blotting experiments. As a first step, we compared the immunoreactivity of hippocampal protein extracts to that of known concentrations of purified protein standards for GLAST and GLT-1. We performed this analysis on samples collected from mice aged 2-3 weeks, 7-8 weeks (the same age of rats from which previous estimates of GLAST and GLT-1 surface density were obtained [28]) and 15 months, to determine how the concentration of these proteins varies at different ages. Briefly, we extracted the membrane proteins from each hippocampal sample, and determined the total membrane protein concentrations using a Bradford assay. We then generated a standard curve to measure the immunoreactivity of dot blots from known amounts of purified, recombinant proteins of the human homologs of GLAST and GLT-1 (**Figure 1**). On the same membranes, we spotted hippocampal membrane protein extracts from mice in each age cohort. Using the standard curve, the RID of each sample dot was converted to moles of GLAST or GLT-1 (**Figure 1A-D**).

We used the dot blot results to estimate on the surface density of each glutamate transporters in mouse hippocampal astrocytes (**Figure 1E,F**). Like [28], we assumed that: (i) the mouse hippocampus contains  $\sim 97.8$  mg/Kg proteins [49]; (ii) it has a density of  $1.05$  g/cm<sup>3</sup> [50]; (iii) GLAST and GLT-1 are mostly expressed in astrocytes; (iv) the molecular weights of GLAST and GLT-1 are 59,619 Da and 62,027 Da, respectively [51,52]. In rats, the astrocytic membrane density is  $1.4$   $\mu\text{m}^2/\mu\text{m}^3$  [53,54]. We tested whether these measures held true for the mouse hippocampus. To do this, we identified astrocytic processes in *stratum radiatum* of the mouse hippocampus using 3D axial STEM tomography, which allowed us to analyze a tissue block of  $\sim 18$   $\mu\text{m}^3$  volume (**Figure 2A**). We traced the contours of astrocytic processes manually (**Figure 2B**), to generate 3D reconstructions (**Figure 2C**) [40,48]. This allowed us to estimate the total surface area of the astrocytic processes in this tissue block and their radius ( $0.075 \pm 0.003$   $\mu\text{m}$ ; mean $\pm$ SD, n=72; **Table 3**). The astrocyte membrane density in the reconstructed block was  $3.15$   $\mu\text{m}^2/\mu\text{m}^3$ , which is more than two times larger than those obtained from the rat hippocampus [53,54]. We used this estimate of astrocytic membrane density to calculate the surface density of glutamate transporters in our tissue samples. The amounts of transporter proteins as percent of total tissue proteins and the tissue concentrations of glutamate transporters are shown in **Tables 4 - 5**, respectively.

## Varying the glutamate transporter surface density alters extrasynaptic receptor activation

The estimates reported in **Table 4** indicate that GLAST and GLT-1, together, contribute 4.16-9.10% of all hippocampal proteins within the age range of the mice used for our experiments. This value is 2.6-5.6 higher than those previously reported for 7-8 week old rats [28]. Together, GLAST and GLT-1 comprise 11-27% of all membrane proteins. Our estimates of glutamate transporter surface density were 1.2-2.7 times higher than previous ones in rats [28] (**Table 5**). These findings prompted us to ask whether this discrepancy is physiologically relevant for regulating glutamate receptor activation at hippocampal synapses. To address this, we generated a 3D reaction-diffusion Monte Carlo simulation (**Figure 3**). Our simulation environment consisted of a  $27$   $\mu\text{m}^3$  cube (the world) containing 7 adjacent synapses positioned at the corners of a regular hexagon (**Figure 3A, left**). The pre- and post-synaptic terminals were modelled as hemispheres with 250 nm radius, separated by a 20 nm high synaptic cleft [55] (**Figure 3A, right**). The edge-to-edge distance between the terminals was 500 nm, consistent with anatomical estimates at hippocampal synapses [22].

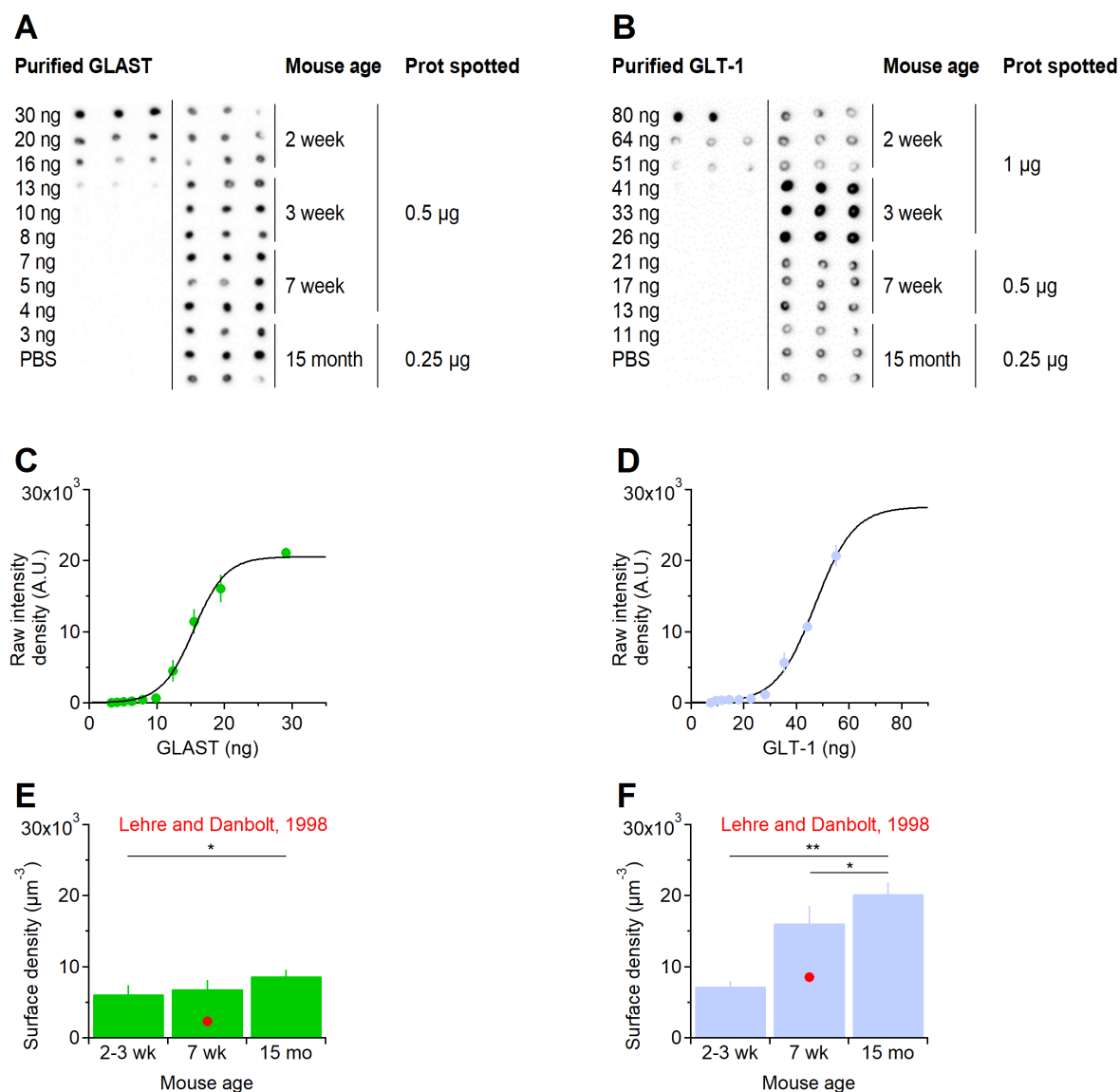


**Figure 1: Dot blot analysis of GLAST and GLT-1 expression in the mouse hippocampus.** **A.** Dot blots of recombinant and native GLAST in hippocampal membrane protein extracts from mice aged 2 weeks - 15 months. **B.** As in A, for GLT-1. **C.** Sigmoidal fit of dot intensity for different amounts of recombinant GLAST. **D.** As in C, for GLT-1. **E.** Estimates of GLAST surface density expression in hippocampal astrocytes of mice aged 2 weeks - 15 months. The red dot represents the results obtained in previous estimates from 7-8 week old rats [28]. **F.** As in E, for GLT-1.

Four of the seven synapses (i.e. 57% [4]) were flanked by astrocytic processes, which covered 43% of their perimeter [4]. At time  $t = 0$ , we released 2,000 glutamate molecules from the center of the synaptic cleft of the synapse at the center of the hexagonal array. Glutamate diffused within the cleft with an apparent diffusion coefficient  $D^* = 3.30e^{-6} \text{ cm}^2/\text{s}$  in the cleft, and  $D^* = 1.29e^{-6} \text{ cm}^2/\text{s}$  outside the cleft, to account for the tortuosity of the hippocampal neuropil ( $\lambda=1.6$ ) [24]. We measured how the glutamate concentration changed over time in and out of the synaptic cleft, using different values for the surface density of astrocyte glutamate transporters (100-20,000  $\mu\text{m}^{-2}$ ). We used these estimates to estimate the probability for each transporter of being in the outward-facing unbound state (To; *magenta*), the outward-facing bound state (ToG; *yellow*) or the inward-facing

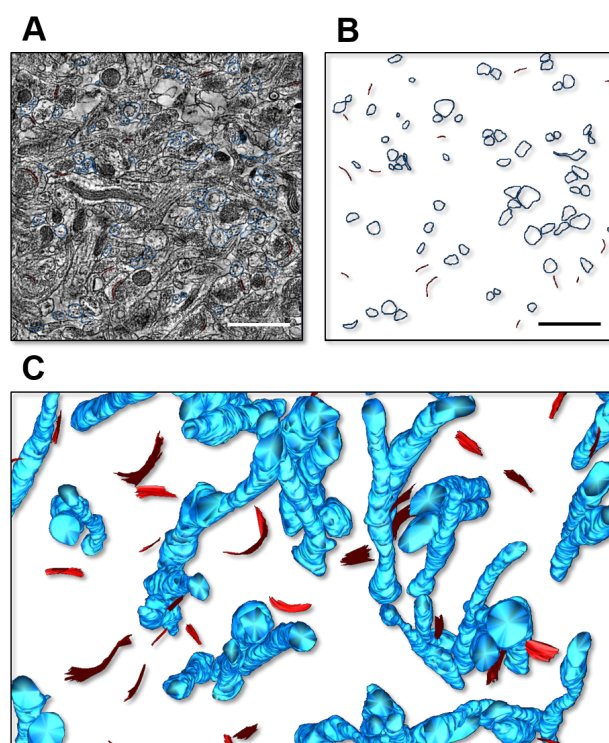


**Figure 2: 3D Axial STEM tomography analysis of astrocytic processes in the mouse hippocampus.** **A.** Example of a single plane of the reconstructed block of tissue, with contours of astrocytic processes (*blue*) and post-synaptic density (PSD; *red*). Scale bar: 1  $\mu$ m. **B.** As in B, without the electron microscopy data. **C.** 3D representation of the astrocytic processes and PSD regions in a portion of the reconstructed tissue block.

	age	% total hipp prot	% mem hipp prot
GLAST	2-3 wk	1.9% $\pm$ 0.4%	4.7% $\pm$ 0.4%
	7 wk	2.1% $\pm$ 0.4%	5.0% $\pm$ 0.5%
	15 mo	2.6% $\pm$ 0.3%*	7.9% $\pm$ 0.5%**
GLT-1	2-3 wk	2.3% $\pm$ 0.2%	6.3% $\pm$ 0.3%
	7 wk	5.1% $\pm$ 0.8%***	13.2% $\pm$ 0.4%*
	15 mo	6.5% $\pm$ 0.5%***	19.1% $\pm$ 0.8%**
All	2-3 wk	4.2% $\pm$ 0.4%	11.0% $\pm$ 0.4%
	7 wk	7.2% $\pm$ 0.8%	18.2% $\pm$ 0.5%
	15 mo	9.1% $\pm$ 0.5%	27.0% $\pm$ 0.8%

**Table 4: Transporter proteins as percent of total and membrane hippocampal proteins.** The amount of each glutamate transporter in mouse hippocampal membranes was determined by quantitative dot blot as described in the Methods section. The percentage of total hippocampal protein composed of each transporter was calculated assuming that there are 97.8 g of protein per kg of tissue (mean  $\pm$  SD;  $n = 3 - 6$ ). The rows labelled “All” represent the sum of the GLAST and GLT-1 measures.

bound state (TiG; *green*; **Figure 3B**). The higher the surface density of glutamate transporters, the higher the glutamate uptake capacity of astrocytes. Therefore, the proportion of transporters in each of the three states decreased for higher values of the glutamate transporter surface density

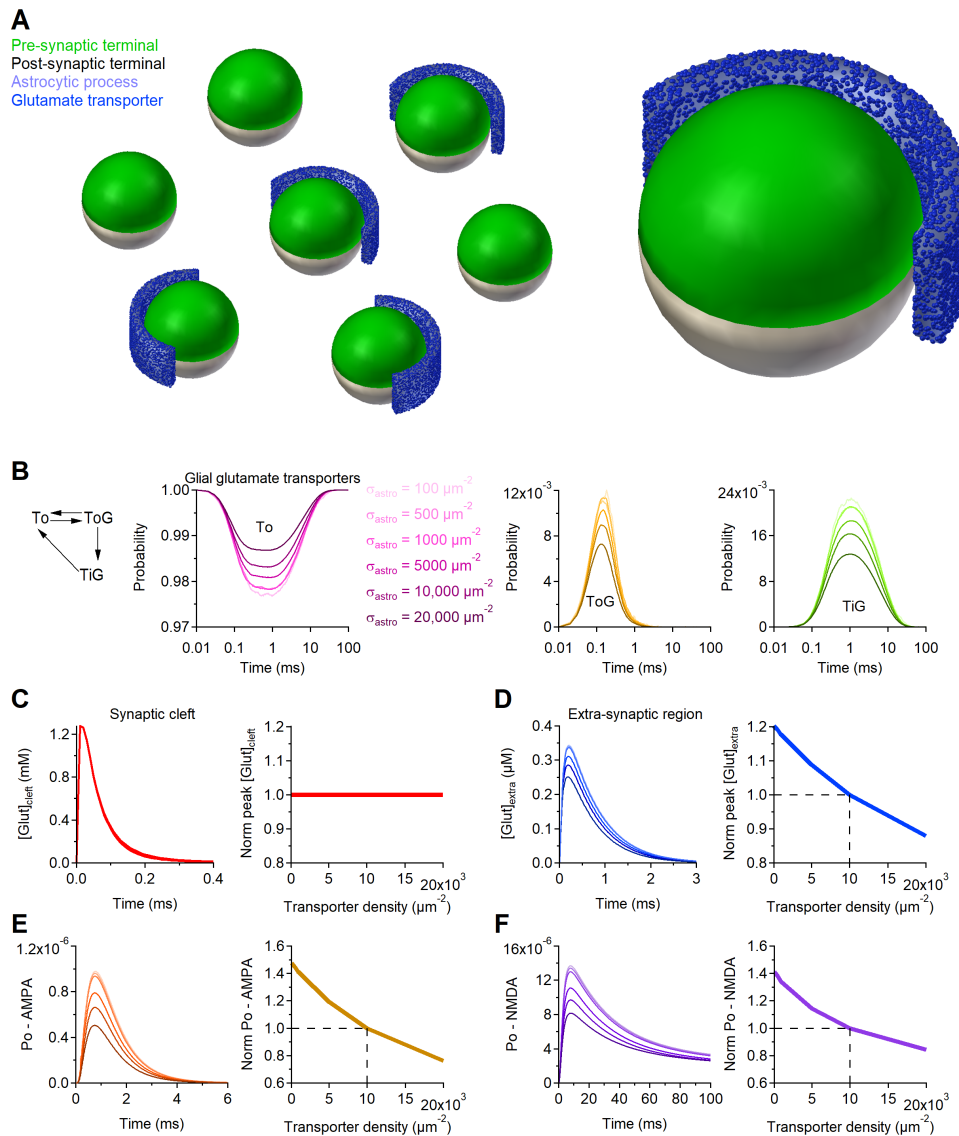
	age	mg transp / g hipp tissue	$\mu\text{M}$	molec / $\mu\text{m}^3$	$\mu\text{m}^2 /$ $\mu\text{m}^3$	molec / $\mu\text{m}^2$
GLAST	2-3 wk	$1.86 \pm 0.37$	$32.0 \pm 6.4$	$19,248 \pm 3,845$	3.15	$6,110 \pm 1,220$
	7 wk	$2.08 \pm 0.37$	$35.8 \pm 6.4$	$21,620 \pm 3,915$	3.15	$6,841 \pm 1,224$
	15 mo	$2.64 \pm 0.26$	$45.4 \pm 4.5$	$27,360 \pm 2,728$	3.15	$8,676 \pm 856$
GLT-1	2-3 wk	$2.30 \pm 0.24$	$37.8 \pm 3.9$	$22,739 \pm 2,319$	3.15	$7,222 \pm 738$
	7 wk	$5.13 \pm 0.76$	$84.1 \pm 12.5$	$50,647 \pm 7,522$	3.15	$16,086 \pm 2,390$
	15 mo	$6.46 \pm 0.52$	$106.0 \pm 8.5$	$63,838 \pm 5,102$	3.15	$20,270 \pm 1,623$
All	2-3 wk	$4.16 \pm 0.37$	$69.8 \pm 6.4$	$41,987 \pm 3,845$	3.15	$13,332 \pm 1,220$
	7 wk	$7.21 \pm 0.76$	$119.9 \pm 12.5$	$72,267 \pm 7,522$	3.15	$22,927 \pm 2,390$
	15 mo	$9.10 \pm 0.52$	$151.4 \pm 8.5$	$91,198 \pm 5,102$	3.15	$28,946 \pm 1,623$

Table 5: **Tissue concentrations of glutamate transporters.** The number of molecules of GLAST or GLT-1 per volume of hippocampal tissue and per cell membrane area were calculated from the dot blot experiment using the following assumptions: the mouse hippocampus contains 97.8 g of protein per Kg of tissue [49], has a density of  $1.05 \text{ g/cm}^3$  [50], and that the molecular weigh of GLAST and GLT-1 are 59,619 and 62,027 Da, respectively (mean  $\pm$  SD;  $n = 3 - 6$ ). The rows labelled “All” represent the sum of the GLAST and GLT-1 measures.

(**Figure 3B**). An increase in astrocytic glutamate transporter expression did not lead to changes in the glutamate concentration profile in the synaptic cleft (**Figure 3C**). Here, glutamate diffusion is the main determinant for the progressive decline in the extracellular glutamate concentration [24]. By contrast, the extrasynaptic glutamate concentration profile became progressively smaller as the glutamate transporter concentration in astrocytic membranes increased (**Figure 3D**). This led to a sharp decrease in the open probability of extrasynaptic AMPA (**Figure 3E**) and NMDA receptors (**Figure 3F**). Together, these results indicate that changes in the surface density of glutamate transporters alter profoundly the activation of extra-synaptic AMPA and NMDA receptors, with potential consequences on synaptic plasticity.

### An evaluation of glutamate transporter surface density based on their non-uniform distribution along the astrocyte membrane

A number of studies suggest that glutamate transporters have a non-uniform distribution along the plasma membrane of astrocytes, and a rapid recycling rate from intracellular compartments [2, 3, 53, 56–58]. Their expression is often described as punctate, with regions where transporters are enriched and exhibit lower lateral mobility confined to the fine tips of astrocytic processes [2, 53, 56–58]. Different glutamate transporter variants display marked differences in their sub-cellular localization [59]. For example, GLAST is localized to both plasma membrane and endoplasmic reticulum and tends to be excluded from astrocytes fine processes, where its expression is 0.6-fold of that at the soma [59]. The expression ratio of GLAST between the astrocytes tip:shaft:stem is 0.8:0.6:1 (here, the stems represent the *GFAP*<sup>+</sup> primary and secondary branches, whereas the shafts represent all other regions of the astrocyte plasma membrane [60]). This means that the tip:shaft:stem:soma ratio with respect to the soma is 0.6:0.5:0.8:1. In contrast, GLT-1 is primarily localized to the plasma membrane, with a 2.3-fold higher expression in fine processes compared to the soma [59]. For GLT-1, the expression ratio at the astrocyte processes tip:shaft:stem processes is 3.2:2:1 [59]. Therefore, the tip:shaft:stem:soma ratio with respect to the soma is 2.3:1.4:0.7:1. Although the astrocyte tips are in contact with excitatory synapses (though not all), this does not mean that other portions of the astrocyte plasma membrane cannot also form contacts with excitatory synapses. This makes room for an interesting consideration: that the average surface density measures for



**Figure 3: Changing the glutamate transporter surface density alters extra-synaptic receptor activation.** **A.** 3D representation of the geometries of seven neighboring synapses used to run the Monte Carlo model. The right panel shows a close-up view of a synapse, composed of a hemispheric pre- (green) and post-synaptic terminal (white), and with 57% of its perimeter surrounded by an astrocytic process, populated with glutamate transporters (blue). **B.** Kinetic scheme of glutamate transporters, with the following kinetic rates:  $k_{To} \rightarrow k_{ToG} = 18e6 M^{-1}s^{-1}$ ;  $k_{ToG} \rightarrow k_{To} = 3,594 s^{-1}$ ,  $k_{ToG} \rightarrow k_{TiG} = 6e3 s^{-1}$ ,  $k_{TiG} \rightarrow k_{To} = 150 s^{-1}$ . The three graphs in this panel provide a description of the probability for each transporter of being in one of the three states  $To$ ,  $ToG$  or  $TiG$ . The results are obtained using a range of transporter surface density  $\sigma_{astro}$ , as shown in the legend. Darker colors represent higher values of  $\sigma_{astro}$ . **C.** Temporal profile of the glutamate concentration in the synaptic cleft for different levels of  $\sigma_{astro}$ , before (left) and after peak normalization of the results obtained when  $\sigma_{astro} = 10,000 \mu m^{-2}$  (right). **D.** As in C, for the extra-synaptic region. **E.** Open probability of extra-synaptic AMPA receptors evoked using the glutamate concentration profiles shown in D (left). The results describing the peak AMPA receptor open probability are normalized by the results obtained when  $\sigma_{astro} = 10,000 \mu m^{-2}$  (right). **F.** As in E, for NMDA receptors.

GLAST and GLT-1 that we derived from our dot blot experiments (**Table 5**) can be refined based on the known variations in the expression of each transporter variants across different sub-cellular



compartments. The results, shown in **Table 6**, indicate how different the concentration of transporters is in the tips, shafts, stems and soma. This suggests that the identity of the astrocyte sub-cellular compartment in contact with a synapses, not only the extent of its synaptic coverage, is a key determinant of extrasynaptic receptor activation at each synapse. Synapses with the same levels of astrocyte coverage can experience various levels of spillover, where the maintenance of the specificity of synaptic transmission is dependent on which sub-cellular compartment reached the synapse.

	Age	tip	shaft	stem	soma
GLAST	2-3 wk	5,057 $\pm$ 1,010	4,214 $\pm$ 841	6,742 $\pm$ 1,346	8,428 $\pm$ 1,683
	7 wk	5,662 $\pm$ 1,013	4,718 $\pm$ 844	7,549 $\pm$ 1,351	9,436 $\pm$ 1,688
	15 mo	7,180 $\pm$ 708	5,983 $\pm$ 590	9,574 $\pm$ 945	11,970 $\pm$ 1,181
GLT-1	2-3 wk	12,300 $\pm$ 1,257	7,489 $\pm$ 765	3,745 $\pm$ 383	5,350 $\pm$ 547
	7 wk	27,410 $\pm$ 4,072	16,680 $\pm$ 2,479	8,341 $\pm$ 1,239	11,920 $\pm$ 1,770
	15 mo	34,530 $\pm$ 2,765	21,020 $\pm$ 1,683	10,510 $\pm$ 842	15,010 $\pm$ 1,202
All	2-3 wk	17,357 $\pm$ 1,257	11,703 $\pm$ 841	10,487 $\pm$ 1,346	13,778 $\pm$ 1,683
	7 wk	33,072 $\pm$ 4,072	21,398 $\pm$ 2,479	15,890 $\pm$ 1,351	21,356 $\pm$ 1,770
	15 mo	41,710 $\pm$ 2,765	27,003 $\pm$ 1,683	20,084 $\pm$ 945	26,980 $\pm$ 1,202

Table 6: **Spatial gradient of glutamate transporter expression in different sub-cellular compartments.** The data, expressed in  $\mu\text{m}^{-2}$ , were calculated using the surface density values from **Table 5**, using distribution ratios in the tip:shaft:stem:soma of 0.6:0.5:0.8:1 and 2.3:1.4:0.7:1 for GLAST and GLT-1, respectively (mean  $\pm$  SD;  $n = 3 - 6$ ). Therefore, the weighted average of the data relative to each compartment corresponds to values shown in **Table 5**. The rows labelled “All” represent the sum of the GLAST and GLT-1 measures.

## A quantitative analysis of the morphology of mouse hippocampal astrocytes

We wanted to determine which proportion of the astrocytic membrane is contributed by the tips, shafts, stems and soma. This can be done more readily using an *in silico* model of astrocytes that captures the main morphological features of real astrocytes. To accomplish this, we first analyzed the morphological properties of biocytin-filled mouse hippocampal astrocytes processed using proExM, visualized with 2P-LSM and scaled to their real size using a correction for linear expansion (see Methods). From the reconstruction of this astrocyte, we estimated the volume of the astrocyte occupied by all its processes (astrocyte cytoplasm), the volume of the neuropil occupied by the astrocyte (astrocyte boundary), and the structure of its branching processes (**Figure 4A**). The branching levels we defined according to the color code shown in **Figure 4C**. The average volume of the neuropil occupied by an astrocyte was  $5.9e^5 \pm 0.6e^5 \mu\text{m}^3$ , whereas the average astrocyte cytoplasmic volume was  $2.1e^5 \pm 0.4e^5 \mu\text{m}^3$  ( $***p = 1.8e^{-4}$ ). The volume occupied by the branch approximation of the astrocyte, which provided a lower bound for the cytoplasmic volume, was  $0.9e^5 \pm 0.9e^5 \mu\text{m}^3$  ( $n=10$ ), and was significantly smaller than that of the astrocyte boundary ( $***p = 2.3e^{-5}$ ) and cytoplasm ( $p=5.1e^{-3}$ ; **Figure 4E, left**). The area of the astrocyte boundary was  $5.4e^4 \pm 0.4e^4 \mu\text{m}^2$ , smaller than the astrocyte cytoplasmic surface area ( $4.0e^6 \pm 0.6e^6 \mu\text{m}^2$ ;  $***p = 3.7e^{-4}$ ) and of the surface area of the branches ( $1.2 \pm 0.2 \mu\text{m}^2$  ( $n=10$ ),  $**p = 2.2e^{-3}$ ;  $**p = 1.6e^{-3}$  between cytoplasm and branch surface area; **Figure 4C, middle**). On average, in each astrocyte, the cumulative length of all branches was  $24.4e^3 \pm 3.8e^3 \mu\text{m}$ , with  $2.2e^3 \pm 0.4 \mu\text{m}^2$  branching points and  $8.5 \pm 0.4$  branch levels (**Figure 4C, right**). A more detailed analysis was performed to derive a 3D Sholl analysis (**Figure 4F, left**) and a count of number of branches for each branching level (**Figure 4F, right**), as well as the branch length (**Figure 4H, left**) and



branching angle from the parent process for each branch level (**Figure 4H, right**). We used these measures as our reference to build an *in silico* model of astrocytes (**Figure 4B**). At each branching point, in the model, the daughter branch had a smaller mean diameter and higher branch level than the parent branch, while the parent branch became thinner but maintained the same branch level (**Figure 4D**). The average cytoplasmic volume, surface area, total branch length, number of branching points and branch levels are shown as scatter plots in (**Figure 4E**). The model provided an accurate description of the Sholl profile (**Figure 4G, left**), number of branches (**Figure 4G, right**), branch length (**Figure 4I, left**) and branching angle for each branch level (**Figure 4I, right**). In this model, which captured numerous features of the real astrocytes, the astrocyte tips, shaft, stems and soma represented 0.3%, 68.1%, 29.8% and 1.9% of the cell membrane. Therefore, the vast majority of the astrocyte membrane has a surface density for glutamate transporters that is 80% than that at the tips for GLAST and 60% for GLT-1 (see also **Figure 10A**).

## The maximal density of glutamate transporters in a 2D circle

With these estimates in mind, we ultimately wanted to determine which fraction of the surface area of different sub-cellular compartments is occupied by glutamate transporters and how their surface density compares with the maximal density of transporters that can be reached in each compartments. Answering this questions requires the use of a geometrical approach, first implemented using simplified 2D and 3D geometries. For example, we can use a circle as a 2D approximation of the astrocyte soma and the cross-section of its branches, and a rectangle with a base  $\omega = 8$  and height  $h = 6.5$  to represent each transporter trimer each trimer as a rectangle (**Figure 5A,B**). This approximation is based on a simplified description of the crystal structure of *Glt<sub>Ph</sub>*, a prokaryotic homolog of glutamate transporters from *Pyrococcus horikoshii* [16].

In a circle delimited by an ideal  $\psi = 3$  nm thick lipid bilayer [61], the distance from the center to the outer layer of the plasma membrane is defined as the outer radius  $r_1$ , whereas  $r_0$  represents the distance from the center to the inner layer of the membrane, where  $r_0 = r_1 - \psi$ . The outer radius of the circle  $r_1$  was allowed to vary, accounting for variability in the size of the soma and of the branch diameters. According to crystal structure analysis of the inward- and outward-facing configurations of *Glt<sub>Ph</sub>*, the transmembrane-spanning portion of each trimer lies approximately half way through the plasma membrane [16, 17, 62]. However, there are conformational changes that occur as glutamate transporters transition between the outward- and inward-facing configuration, which allow the transporter to protrude towards the cytoplasm ( $h_{in} = 3.5$  nm) or towards the extracellular space ( $h_{in} = 0$  nm) [17, 20, 62–65]. For this reason, in our analysis, we include the results obtained for  $h_{in} = 0$  (transporters protruding towards the extracellular space), 1.75 (transporters located half-way through the plasma membrane) and 3.5 nm (transporters protruding towards the cytoplasm). For our further computations, we also used the distance from the outside surface of the soma to the inward bottom of the trimer  $h_{out}$ , defined as follows:

$$h_{out} = h_{in} + \psi \quad (10)$$

Therefore,  $h_{out}$  could vary between  $\psi = 3$  nm (when  $h_{in} = 0$ ) and  $h_{out} = 6.5$  nm (when  $h_{in} = 3.5$  nm). Having defined these parameters, we proceeded to estimate the maximum number of transporter trimers that can be fitted in the circle ( $n_{circle}$ ), as well as their maximal linear density ( $\sigma_{circle}$ ) and the maximal fraction of perimeter occupancy ( $\phi_{circle}$ ; **Figure 6**). The corresponding values for the transporter monomers was estimated by multiplying these values by three.

The maximum number of transporter trimers that can occupy a circle  $n_{circle}$  depends on: (i) the circumference of the circle (i.e., on  $r_1$ ); (ii) the transporter trimer width  $\omega$ ; and (iii) the height of the transporter trimer protruding in the cytoplasm ( $h_{in}$ ). For a fixed cytoplasmic protrusion

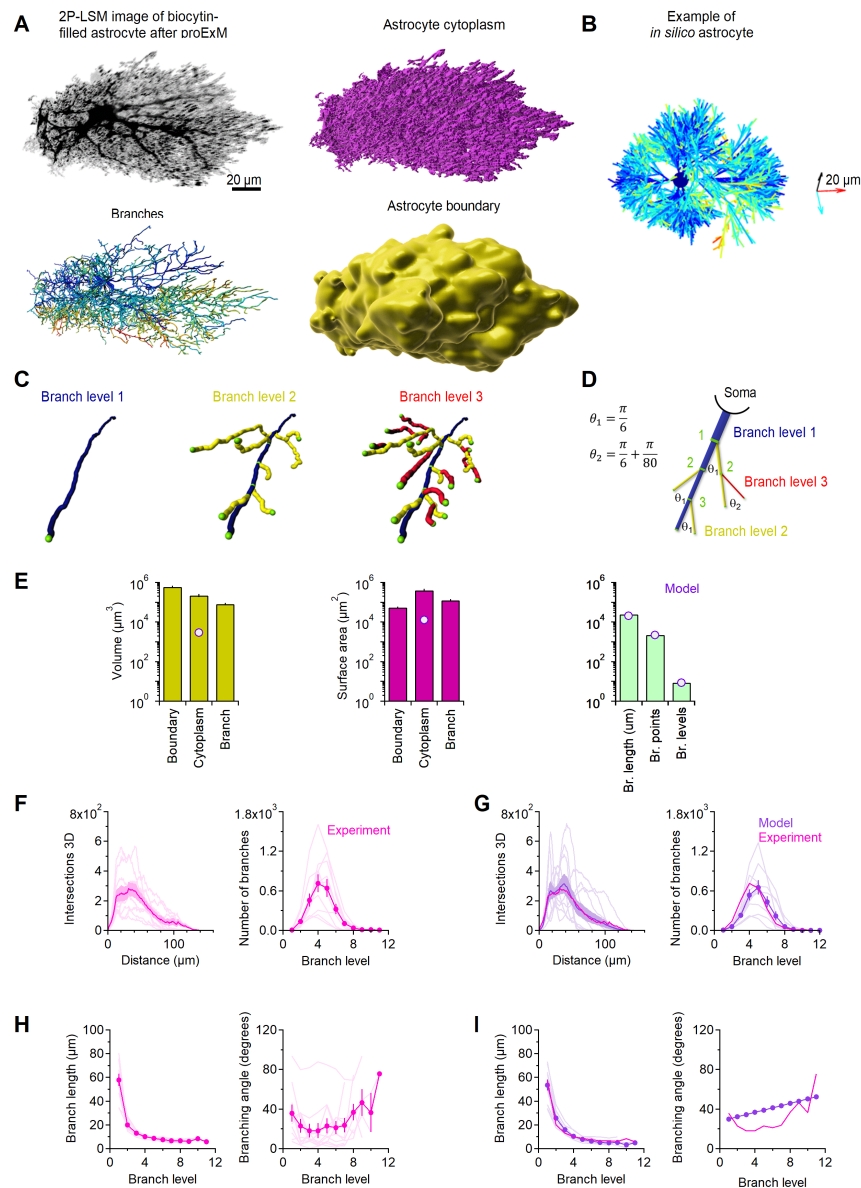


**Figure 4: Astrocyte in *stratum radiatum* of the mouse hippocampus.** **A.** *Top left*, Maximum intensity projection of a 2P-LSM z-stack of a biocytin-filled astrocyte in a mouse hippocampal *stratum radiatum*. *Top right*, Image analysis of astrocytic branches. Higher branching levels are denoted by warmer colors. *Bottom left*, Image analysis of astrocyte cytoplasm. *Bottom right*, Volume of the hippocampal neuropil occupied by the astrocyte. **B.** *In silico* representation of an astrocyte generated through our MATLAB model. The color scheme for each branch level is the same used for the reconstructions of biocytin-filled astrocytes shown in panel A. The scale bar is 20  $\mu\text{m}$  in the x (cyan), y (red) and z axis (black). **C.** Color-coded representation of branching levels of progressively higher order. **D.** As in C, for the *in silico* data. **E.** Summary analysis of volume (*left*) and surface area analysis (*middle*) of the cell bounding volume, cytoplasm and branches. The histogram on the right provide a quantitative analysis of branch length, number of branch points and branch levels across all analyzed astrocytes. **F.** Sholl analysis (*left*) and summary of branch count analysis for different branch levels (*right*). **G.** As in G, for the *in silico* data. **H.** Summary analysis of branch length (*left*) and branching angle (*right*) for each branching level. **I.** As in G, for the *in silico* data.

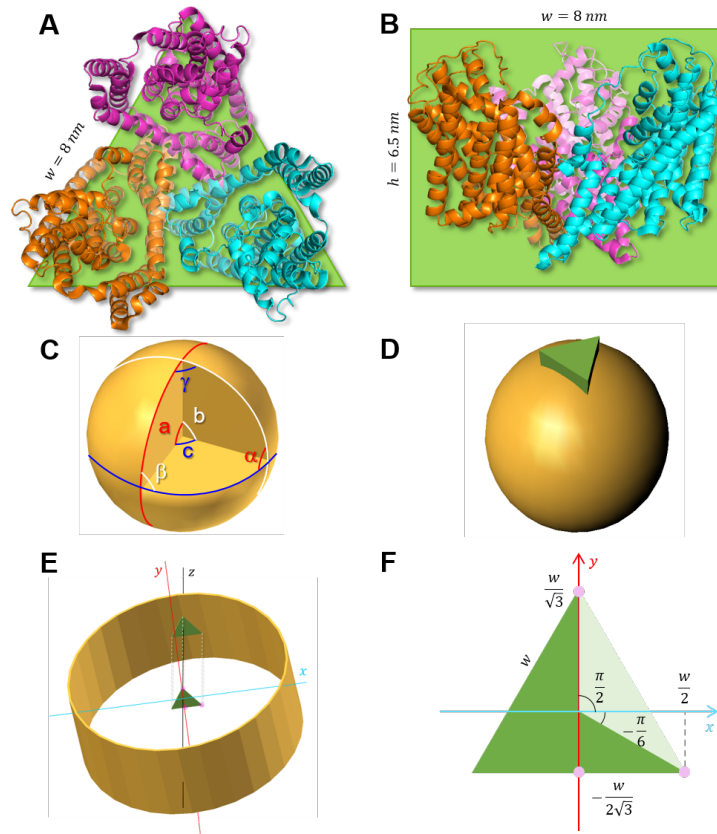


**Figure 5: Geometrical approximations used for modeling transporters.** **A.** Extracellular view of the ribbon representation of a *Glt<sub>Ph</sub>* trimer, with protomers shown in orange, magenta and cyan. The green triangle with side length  $w = 8$  nm is used to approximate the cross section of the trimer. **B.** View of the trimer parallel to the membrane. The green rectangle with  $h = 6.5$  nm height is used to approximate the side view of the trimer. **C.** Spherical triangle (formed by three intersecting lunes) with spherical angles  $\alpha$ ,  $\beta$  and  $\gamma$ , corresponding to angles at the center of the sphere called  $a$ ,  $b$  and  $c$ , respectively. **D.** Schematic representation of a trimer (green prism) protruding through the plasma membrane of a spherical compartment. **E.** Schematic representation of a transporter protruding inside a cylindrical compartment; the bottom of the trimer and its projection onto the  $x, y$  Cartesian coordinate plane are shown as green triangles. **F.** Projection of the trimer onto the coordinate plane, used as the domain for computing the double integrals for  $A_{sphere}^{\Delta}$  and  $A_{cyl}^{\Delta}$ .

$h_{in}$  and when  $r_1 > h_{out}$  (so that the circle can accommodate at least two trimers), the number of trimers can be maximized by placing them in a radially symmetric fashion around the circle of radius  $r_1$ , such that their inner widths delimits a regular polygon concentric with the center of the circle. Then  $n_{circle}$  is precisely the number of sides of this polygon. To estimate  $n_{circle}$ , we additionally labelled the distance  $r_{-1}$  from the center to the corners of the polygon, and the distance  $l$  from the center to the sides of the polygon (**Figure 6A**). By applying Pythagoras' rule to the triangles delimited by  $(r_{-1}, l, \omega/2)$  and  $(r_1, l + h_{out}, \omega/2)$ , we obtained:

$$r_{-1}^2 = l^2 + \left(\frac{\omega}{2}\right)^2 \quad (11)$$

and

$$r_1^2 = (l + h_{out})^2 + \left(\frac{\omega}{2}\right)^2 \quad (12)$$

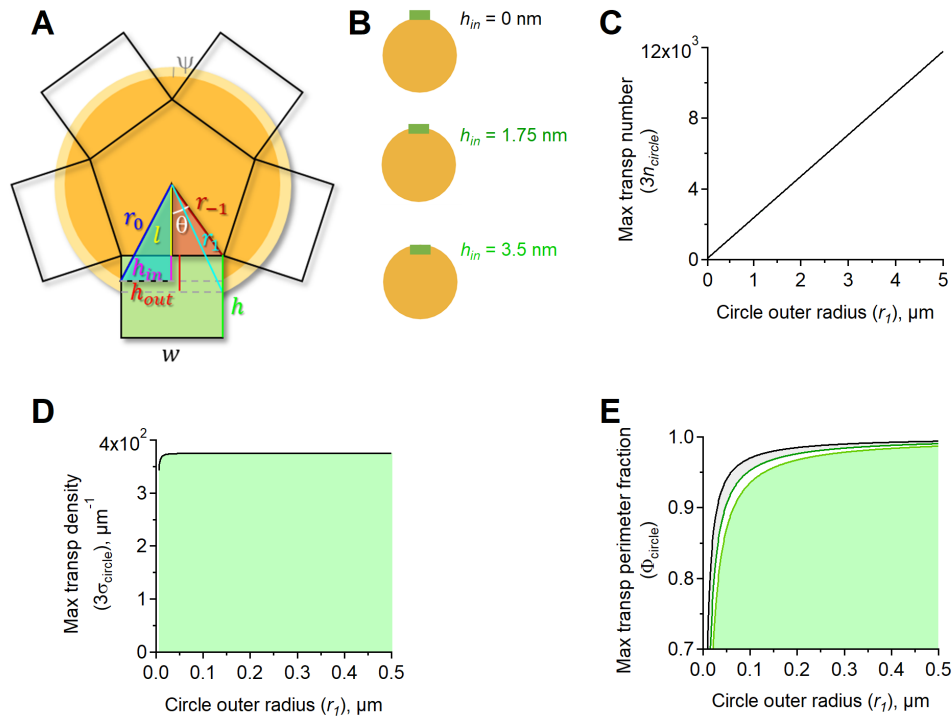


**Figure 6: Spatial relationship between adjacent glutamate transporter trimers in a circle.** **A.** Each transporter trimer had a portion of length ( $h_{in}$ ) that could protrude inside the circle from the cytoplasmic layer of the plasma membrane. The side length of the trimers was  $\omega = 8$  nm. This spatial arrangement provided a framework to estimate the maximum number of transporter trimers and monomers that can reside in the perimeter of a circle ( $n_{circle}$ ) of radius  $r_1$ . **B.** Schematic representation of circles with transporter trimers. The glutamate transporter trimers were represented as rectangles with 8 nm side length and 6.5 nm height. The example at the top refers to trimers that do not protrude into the circle. In the example in the middle, the trimers were located half way through the plasma membrane and protruded in the circle by 1.75 nm. In the case described at the bottom, the trimers protruded all the way through the membrane, for 3.5 nm. **C.** Estimates of the maximum number of transporter molecules ( $3n_{circle}$ ) that can be positioned along the circumference of circles of different radius  $r_1$ . We examined the three different cases described in (A), where  $h_{in} = 0$  nm (black),  $h_{in} = 1.75$  nm (dark green) and  $h_{in} = 3.5$  nm (light green). **D.** Estimates of the 2D glutamate transporter monomer density for each value of  $h_{in}$ . **E.** Proportion of the circle perimeter occupied by transporter monomers for increasing values of the circle radius. An asymptotic value of 1 was reached at varying rates depending on the value of  $h_{in}$ .

By subtracting Equation (11) from Equation (12), we obtained:

$$r_1^2 - r_{-1}^2 = 2lh_{out} + h_{out}^2 \quad (13)$$

We expressed  $l = r_{-1} \cos(\theta)$  and  $\omega = 2r_{-1} \sin \theta$ , where the angle  $\theta = \frac{\pi}{n_{circle}}$  can vary in the range  $[0, \pi/2]$  (**Figure 6A**). As a result, Equation (13) can be re-written as:

$$r_{-1}^2 + 2r_{-1}h_{out} \cos \theta + h_{out}^2 - r_1^2 = 0 \quad (14)$$

By eliminating  $r_{-1} = \omega/(2 \sin \theta)$ , Equation (14) can also be re-written as:

$$\frac{\omega^2}{4 \sin^2 \theta} + h_{out} \omega \cot \theta - r_1^2 + h_{out}^2 = \frac{\omega^2}{4} [\cot^2 \theta + 1] + h_{out} \omega \cot \theta - r_1^2 + h_{out}^2 = 0 \quad (15)$$

This led to the quadratic equation in  $\xi = \cot \theta$ :

$$\frac{\omega^2}{4}\xi^2 + h_{out}\omega\xi + \frac{\omega^2}{4} - r_1^2 + h_{out}^2 = 0 \quad (16)$$

By solving for  $\xi = \cot \theta > 0$ , we obtained:

$$\cot \theta = \cot \left( \frac{\pi}{n_{circle}} \right) = \frac{-2h_{out} + \sqrt{4r_1^2 - \omega^2}}{\omega} \quad (17)$$

Based on Equation (17), the maximum number of transporter trimers of width  $\omega$  and cytoplasmic protrusion height  $h_{in}$  that can occupy a circle of radius  $r_1$  is:

$$n_{circle} = \frac{\pi}{\cot^{-1} \left( -2h_{out}/\omega + \sqrt{4r_1^2/\omega^2 - 1} \right)} \quad (18)$$

Our computation, and subsequently Equation (18), holds true if  $r_1 > h$  and  $r_1 > \omega/2$  (to allow space for at least two trimer insertions into the astrocyte cytoplasm). These conditions were both satisfied experimentally, given that the radius of the finest tip of the terminal branches of astrocytes were 10-120 nm (**Table 3**). As expected,  $n_{circle}$  increased as  $r_1$  increased (i.e. bigger circles contained more transporters), and the dependence was almost indistinguishable from linear within the conditions for  $r_1$  (**Figure 6B,C**). Increasing  $h_{in}$  values produced no changes in the graph, because any steric effect due to possible collisions between the cytoplasmic tails of adjacent transporters is negligible when  $r_1 > h$  and  $r_1 > \omega/2$  (**Figure 6B,C**). The maximum linear density of transporter trimers  $\sigma_{circle}$ , was calculated by dividing  $n_{circle}$  by the circumference length:

$$\sigma_{circle} = \frac{n_{circle}}{2\pi r_1} \quad (19)$$

Here, the transporter density  $3\sigma_{circle}$  approaches an asymptotic value of  $1/\omega \sim 375 \mu\text{m}^{-1}$ , independently of the value of  $h_{in}$ , and reaches 99% of it when  $r_1 > 17$  nm (**Figure 6D**). The fraction of the circle circumference occupied by the transporters,  $\Phi_{circle}$ , can be calculated as the ratio between the length of the circumference occupied by the trimers  $n_{circle}$  and that of the entire circumference. Here, the circular length occupied by the trimers can be calculated as  $\hat{\omega} = 2\theta r_1 = 2r_1 \sin^{-1} \left( \frac{\omega}{2r_1} \right)$ , and the maximum portion of the circle occupied by them is given by:

$$\Phi_{circle} = \frac{n_{circle}\hat{\omega}}{2\pi r_1} = \frac{n_{circle} \sin^{-1}(\omega/2r_1)}{\pi} = \frac{\sin^{-1}(\omega/2r_1)}{\cot^{-1} \left( -2h_{out}/\omega + \sqrt{4r_1^2/\omega^2 - 1} \right)} \quad (20)$$

The relationship approached the asymptotic value 1, for all values of  $h_{in}$  (**Figure 6E**). This asymptotic value was reached more slowly as  $h_{in}$  increased (i.e. as the transporter trimers protruded more towards the astrocyte cytoplasm). For  $h_{in} = 0, 1.75$ , and  $3.5$  nm, 99% of the asymptotic value was reached when  $r_1 = 300, 475$  and  $650$  nm, respectively. Note that the relationship between  $\Phi_{circle}$  and  $r_1$  was less steep than the relationship between  $\sigma_{sphere}$  and  $r_1$ . This was due to the fact that the dependence of the circle perimeter on  $r_1$  grew more slowly than that of the perimeter length occupied by the monomers as  $r_1$  increased. Together, the results of this simple 2D model indicate that crowding effects do not limit the local surface expression of glutamate transporters in large sub-cellular compartments like the soma, but can do this in small astrocytic processes, depending on the expression of other molecules.

## The maximal density of glutamate transporters in a 3D sphere

A similar conceptual strategy to the one described for the 2D circle can be applied to estimate the glutamate transporter surface density in 3D, using a spherical representation of the astrocyte soma (**Figure 5D**). As in the 2D case, the geometry that maximizes the number of transporters is obtained when the cytoplasmic portions of the trimers touch each other, delimiting the triangular faces of a regular polyhedron with side length  $\omega$ .

For simplicity, we used the same notation system described in the previous section, where  $r_1$  is the external radius of the sphere,  $r_0 = r_1 - \psi$  is the slightly smaller radius of the cytoplasmic portion of the sphere (accounting for the membrane thickness  $\psi$ ), and  $r_{-1}$  is the radius of the sphere that circumscribes the polyhedron described by the cytoplasmic portions of the trimers. Consistent with our previous notation, we called  $h_{in}$  the depth of the cytoplasmic protrusion of the trimer, and  $h_{out} = h_{in} + \psi$  the insertion depth measured from the outer portion of the plasma membrane. The radius  $r_{-1}$  was obtained as a function of  $r_1$ ,  $\omega$  and  $h_{out}$ . If we call  $l$  the distance from the center of the sphere to the cytoplasmic portion of each trimer, we obtain:

$$l = \sqrt{r_{-1}^2 - \omega^2/3} \quad (21)$$

following that:

$$l + h_{out} = \sqrt{r_{-1}^2 - \omega^2/3} + h_{out} = \sqrt{r_1^2 - \omega^2/3} \quad (22)$$

Solving for  $r_{-1}$ , we obtain:

$$r_{-1} = \sqrt{r_1^2 + h_{out}^2 - 2h_{out}\sqrt{r_1^2 - \omega^2/3}} \quad (23)$$

We estimated the number  $n_{\text{sphere}}$  of triangular prisms (i.e. the transporter trimers) distributed along the outer surface of the sphere (**Figure 5F**). Each pair of vertices of each triangle (i.e. the base of the prisms) defines a great circle on the sphere (that is a circle centered at the center of the sphere). Therefore, each triangle defined three great circles (**Figure 5C**). If one calls  $A^{\Delta_s}$  the area of the spherical triangle delimited by these three great circles, then:

$$n_{\text{sphere}} = \frac{4\pi r_{-1}^2}{A^{\Delta_s}} \quad (24)$$

The area  $A^{\Delta_s}$  was computed in the Methods section using a strategy for overlapping spherical lunes, as:

$$A^{\Delta_s} = r_{-1}^2 \left[ 3 \cos^{-1} \left( \frac{2r_{-1}^2 - \omega^2}{4r_{-1}^2 - \omega^2} \right) - \pi \right] \quad (25)$$

Hence the maximum number of transporter trimers that can be placed in a sphere can be approximated by dividing the surface area of a sphere of radius  $r_1$  by  $A^{\Delta_s}$ :

$$n_{\text{sphere}} = \frac{4\pi}{3 \cos^{-1} \left( \frac{2r_1^2 + 2h_{out}^2 - 4h_{out}\sqrt{r_1^2 - \omega^2/3} - \omega^2}{4r_1^2 + 4h_{out}^2 - 8h_{out}\sqrt{r_1^2 - \omega^2/3} - \omega^2} \right) - \pi} \quad (26)$$

The maximum surface density of the trimers can then be expressed by:

$$\sigma_{\text{sphere}} = \frac{n_{\text{sphere}}}{4\pi r_1^2} \quad (27)$$



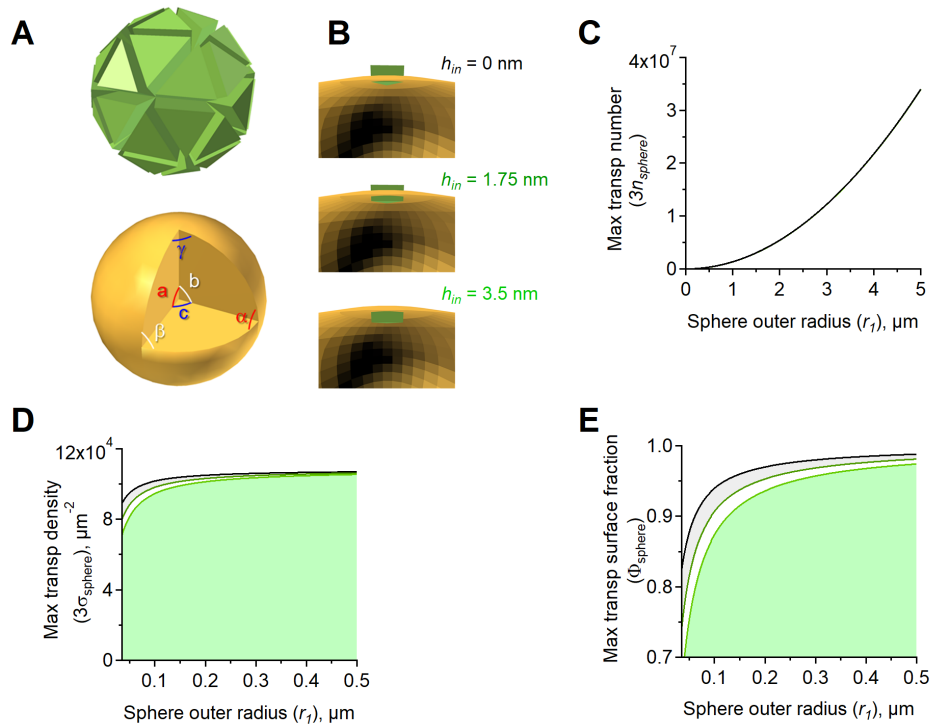


**Figure 7: Spatial relationship between adjacent glutamate transporter trimers in a sphere. A.** *Top*, Spatial distribution of transporter trimers in a sphere. *Bottom*, A spherical triangle is a figure formed on the surface of a sphere by three great circular arcs intersecting pairwise in three vertices. The spherical triangle is the spherical analog of the planar triangle. The figure shows a spherical triangle with angles  $a, b, c$ , equivalent to the angles  $\alpha, \beta, \gamma$ . **B.** Schematic representation of spheres used as 3D representations of the astrocyte soma. Glutamate transporter trimers are represented as prisms with triangular base of 8 nm side length and 6.5 nm height. The example at the top refers to trimers that do not protrude into the sphere. In the example in the middle, the trimers are located half way through the plasma membrane and protrude in the sphere by 1.75 nm. In the case described at the bottom, the trimers protrude all the way through the membrane, for 3.5 nm. **C.** Estimates of the maximum number of transporter trimers  $n_{sphere}$  that can be positioned along the surface of spheres of different radius  $r_1$ . We examined the three different cases described in (B), where  $h_{in} = 0$  nm (black),  $h_{in} = 1.75$  nm (dark green) and  $h_{in} = 3.5$  nm (light green). **D.** Estimates of the 3D transporter trimer surface density for each value of  $h_{in}$ . **E.** Fraction of the surface area of the sphere that can be occupied by transporter trimers.

The number and surface density of transporter monomers can be obtained by multiplying  $n_{sphere}$  and  $\sigma_{sphere}$  by three.

The lateral sides of each transporter trimer cut a spherical triangle of area  $A_{sphere}^{\Delta}$  out of the plasma membrane (i.e. from the sphere of radius  $r_1$ ). The area of this spherical triangle was calculated as a double iterated integral of the spherical surface of radius  $r_1$  over the triangular domain of side length  $w$  centered at the origin. In the Methods section, we used polar coordinates to rewrite this area in terms of a double integral, and compute it as:

$$A_{sphere}^{\Delta}(r_1) = 2\pi r_1^2 - 3r_1^2 \left[ 2 \tan^{-1} \left( \frac{3r_1}{\sqrt{3r_1^2 - \omega^2}} \right) - \frac{\omega}{\sqrt{3}r_1} \sin^{-1} \left( \frac{\sqrt{3}\omega}{\sqrt{12r_1^2 - \omega^2}} \right) \right] \quad (28)$$



Therefore, the maximum fraction of the sphere surface occupied by transporter trimers is:

$$\Phi_{\text{sphere}} = \frac{n_{\text{sphere}} \cdot A_{\text{sphere}}^{\Delta}(r_1)}{4\pi r_1^2} \quad (29)$$

where  $A_{\text{sphere}}^{\Delta}$  is provided by Equation (28). The results of this analysis, summarized in (**Figure 7**), show that the number of transporters on the surface of a sphere increases with the sphere radius  $r_1$ . In this case, however, the relationship increases faster than if it was linear (cf. **Figure 7C** and **Figure 6C**). For a small radius ( $r_1 < 0.1$  nm), the transporter density increased steeply as  $r_1$  got larger, but this behavior eventually tapered off as  $r_1$  increased, eventually approaching an asymptotic value of  $10.8e^4$  monomers  $\mu\text{m}^{-2}$ . As the transporters protruded more towards the astrocyte cytoplasm, the asymptotic value was approached more slowly for increasing values of  $r_1$ . Accordingly, 99% of the asymptotic value was reached at  $r_1 = 488, 768$  and  $1057$  nm, respectively as  $h_{in}$  increased from 0 to 1.75 and 3.5 nm. The relationship between  $n_{\text{sphere}}$  and  $r_1$  was less steep than the one between  $n_{\text{circle}}$  and  $r_1$ , which we described for the 2D case (cf. **Figure 7** and **Figure 6D**). This held true when calculating the proportion of a sphere of increasing radius that can be occupied by the transporters (cf. **Figure 7E** and **Figure 6E**). In this case, 99% of the sphere surface could be occupied by transporter monomers at  $r_1 = 601, 949, 1,298$  nm, respectively, as  $h_{in}$  increased from 0 to 1.75 and 3.5 nm. Together, these results show that changes in the conformational state of glutamate transporters, leading to changes in the insertion level in the plasma membrane, are unlikely to create steric hindrance limits in large sub-cellular compartments like the soma, but can do so in small bulbous protrusions that astrocytes form, especially if their radius is only a few tens or hundreds nm.

### The maximal density of glutamate transporters in a 3D cylinder

Each astrocyte branch, or its portions, can be roughly approximated by a cylinder (**Figure 5E**). Given that the diameter of a branch (i.e. a cylinder) is typically larger than the summed height of two trimers  $2\chi$ , the configuration that maximizes trimer packing along horizontal rings is the one shown schematically in **Figure 8A,B**. Here, a cylinder is formed by a stack of rings, and each ring has height  $H = \sqrt{3}\omega/2$ , which corresponds to the height of the triangular base of a trimer.

If one considers a cross section of a cylinder that is perpendicular to its axis, it is possible to recover the circular geometry of the 2D model described previously, where each rectangle corresponds to a pair of trimers. This observation allowed us to calculate the maximum number of trimers that can be assembled along this cylindrical ring of radius  $r_{cyl}$  as twice the number of rectangles that can fit around the circular cross section of the cylinder, as calculated for a circle:

$$n_{\text{ring}} = \frac{2\pi}{\cot^{-1}\left(-2h_{out}/\omega + \sqrt{4r_{cyl}^2/\omega^2 - 1}\right)} \quad (30)$$

where  $h_{out} = h_{in} + \psi$ . A cylinder of length  $L$  consists of  $L/H = 2L/\sqrt{3}\omega$  stacked rings. Therefore, the total number of trimers along a cylinder of length  $L$  and radius  $r_{cyl} > h_{out}$  is given by:

$$n_{cyl}(r_{cyl}, L) = \frac{2\pi}{\cot^{-1}\left(-2h_{out}/\omega + \sqrt{(2r_{cyl})^2/\omega^2 - 1}\right)} \cdot \frac{2L}{\sqrt{3}\omega} \quad (31)$$

For a given value of  $L$ , the trimer number  $n_{cyl}$  increases approximately linearly **Figure 8C**. The maximum surface density of trimers in a cylinder of length  $L$  can be expressed as:

$$\sigma_{cyl} = \frac{n_{cyl}}{2\pi r_{cyl} L} \quad (32)$$

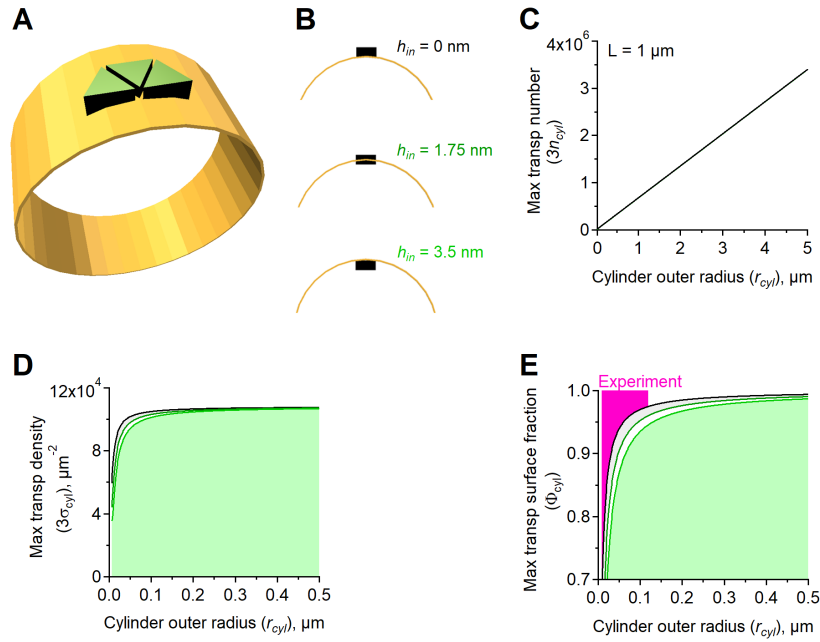


**Figure 8: Spatial relationship between adjacent glutamate transporter trimers in a cylinder.** **A.** Schematic representation of trimer arrangement around the lateral surface of a cylinder. For clarity, we only show three adjacent trimers, but in reality they keep covering the entire lateral surface of the cylinder using the same pattern. **B.** Schematic representation of cylinders used as 3D representations of astrocytic branches. Glutamate transporter trimers are represented as prisms with triangular base of 8 nm side length and 6.5 nm height. The example at the top refers to trimers that do not protrude in the lumen of the cylinder. In the example in the middle, the trimers are located half way through the plasma membrane and protrude inside the cylinder by 1.75 nm. In the case described at the bottom, the trimers protrude all the way through the membrane, for 3.5 nm. **C.** Estimates of the maximum trimer number  $n_{cyl}$  that can be positioned along the lateral surface of cylinders of different radius  $r_{cyl}$  (the height of the cylinder in this case is set to  $L = 1 \mu m$ ). We examined the three different cases described in (B), where  $h_{in} = 0$  (black),  $h_{in} = 1.75$  (dark green) and  $h_{in} = 3.5$  nm (light green). **D.** Estimates of trimer surface density for each value of  $h_{in}$ . **E.** Estimates of the fraction of the lateral surface of the cylinder that can be occupied by trimers for each value of  $h_{in}$ . The area shaded in magenta represents the range of experimental measures for tip diameters.

The maximum monomer density is obtained by multiplying  $\sigma_{cyl}$  by three (**Figure 8D**). Here, the maximum transporter surface density  $3 \cdot \sigma_{cyl}$  approaches an asymptotic value of  $10.82e4 \mu m^{-2}$ . Accordingly, 99% of this asymptotic value is reached at  $r_{cyl} = 282$  nm, 445 nm, and 608 nm, respectively, as  $h_{in}$  increased from 0 to 1.75 and 3.5 nm (**Figure 8D**). Values significantly lower than the asymptotic value could be detected in small cylinders with  $r_{cyl} < 0.1 \mu m$ , meaning that a crowding effect can limit the local surface density of the transporters in very small astrocytic processes whose geometry can be approximated to that of cylinders. The area  $A_{cyl}^{\Delta}(r_{cyl})$  that each trimer occupies on the surface of a cylindrical extension of radius  $r_{cyl}$  was calculated in the Methods section as a double integral:

$$A_{cyl}^{\Delta}(r_{cyl}) = \sqrt{3}\omega r_{cyl} \sin^{-1}\left(\frac{\omega}{2r_{cyl}}\right) + \sqrt{3}r_{cyl}\sqrt{4r_{cyl}^2 - \omega^2} - 2\sqrt{3}r_{cyl}^2 \quad (33)$$

From this formula, we calculated the proportion of the cylindrical surface area occupied by trimers as:

$$\Phi_{cyl} = \frac{n_{cyl}(r_{cyl}, L) \cdot A_{cyl}^{\Delta}(r_{cyl})}{2\pi r_{cyl} L} \quad (34)$$

where  $n_{cyl}(r_{cyl}, L)$  and  $A_{cyl}^{\Delta}(r_{cyl})$  are given by Equations 31 and 33, respectively. The protrusion of the trimers towards the lumen of the cylinder introduced a crowding effect that prevented them from occupying the entire lateral surface of the cylinder. Accordingly, 99% of the asymptotic value 1 was reached at  $r_{cyl} = 302, 476$ , and  $651$  nm, respectively, as  $h_{in}$  increased from 0 to 1.75 and 3.5 nm (**Figure 8E**). This means that astrocytic processes with terminal processes that are only 18-238 nm wide (see **Table 3**) may have an upper limit to the number of transporters they express due to their small size.

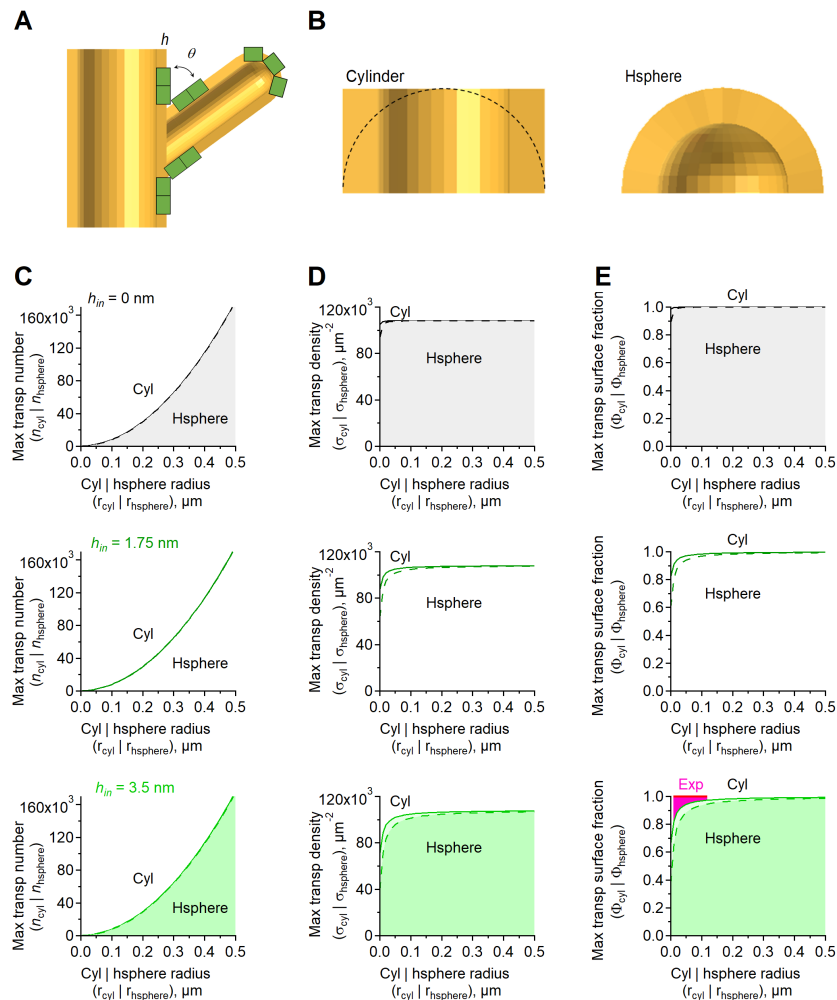


**Figure 9: Geometric constraints on trimer distribution close to branch points.** **A.** The illustration shows in cross section the astrocyte geometry at a branch point and at a branch tip. Each transporter trimer is represented as a green rectangle of height  $h$ . In this specific illustration, the trimer is protruding out of the plasma membrane, but our calculations were performed for  $h_{in}=0-3.5$  nm. The branching points and branch tip are regions that display a crowdedness effect, which reduces the local density of transporter trimers. **B.** Close-up view of the tip of an astrocyte process ending either as a cylinder (*left*) or as a hemisphere (*right*). **C.** Estimates of the maximum trimer number that can be placed in a cylinder with height equals to the radius (*solid line*) or in a hemisphere (*dashed line*), for  $h_{in}=0$  nm (*top*),  $h_{in}=1.75$  nm (*middle*) and  $h_{in}=3.5$  nm (*bottom*). **D.** As in C, for trimer density. **E.** As in C, for the portion of the plasma membrane occupied by transporter trimers.

When assembling multiple cylindrical segments into the 3D simulations of the branching trees, we considered the effects of potential geometric constraints at the branching points. The fact that

the branching angle between the daughter and the parent branch is  $< \pi/2$  means that the daughter branches are not perfect right cylinders. However, the surface area of a daughter branch segment can be approximated with that of an equivalent right cylinder with the same length (measured along the axis of the original branch segment), since the area of each branch segment that is lost or gained at the branch insertion point are roughly equal. This shape also provides an appropriate approximation of the proportion of the surface area occupied by the trimers, accounting for crowding effects caused by potential collisions between the extracellular domains of adjacent trimers (which lead to trimer-free regions at the branching points; **Figure 9**). Taking these constraints into consideration, the area of each branch segment that is lost or gained on the two sides of the branch insertion point are roughly equal. With this in mind, we can simply assume right cylindrical shapes for all branch segments. Hence no further approximations were implemented in our model cell simulations in conjunction with these two constraints.

While the assumption of cylindrical shape can be made for most branch portions, one exception are the tips of terminal branches, which are better approximated by the shape of a small hemisphere. Since the diameters of the terminal branches are typically very small, the additional curvature of the tips makes them another location where spacial constraints are likely to lead to geometric hindrance for trimer distribution. To estimate the size of this effect with our simulations, we considered the small hemispherical tips as a separate model cell compartment (see below). The theoretical transporter number, density and fraction of the membrane occupied by transporters can then be compared between this compartment and other parts of the cell, to infer the effect of the additional geometric constraints present at the tip. As a basic approximation (illustrated in **Figure 9**, and detailed mathematically in Equations (35)-(40)), notice that these measures tightly agree for a hemispherical tip and for a cylindrical tip of the same height (assuming no transporters are placed on the end of the cylindrical portion).

$$n_{htip}(r) = \frac{2\pi}{3 \cos^{-1} \left( \frac{2r^2 + 2h_{out}^2 - 4h_{out}\sqrt{r^2 - \omega^2/3} - \omega^2}{4r^2 + 4h_{out}^2 - 8h_{out}\sqrt{r^2 - \omega^2/3} - \omega^2} \right) - \pi} \quad (35)$$

$$n_{ctip}(r) = \frac{2\pi}{\cot^{-1} \left( -2h_{out}/\omega + \sqrt{4r^2/\omega^2 - 1} \right)} \cdot \frac{2r}{\sqrt{3}\omega} \quad (36)$$

$$\sigma_{htip} = \frac{n_{htip}}{4\pi r^2} \quad (37)$$

$$\sigma_{ctip} = \frac{n_{ctip}}{2\pi r^2} \quad (38)$$

$$\Phi_{htip} = \frac{n_{htip} A_{sphere}^{\Delta}(r)}{4\pi r^2} \quad (39)$$

$$\Phi_{ctip} = \frac{n_{ctip} A_{cyl}^{\Delta}(r)}{2\pi r^2} \quad (40)$$

## Theoretical estimates of transporter surface density in model astrocytes

Now that all the geometric building blocks are in place, we could use them to generate an *in silico* model of astrocytes. Since we have the experimental constraints for the morphology of the astrocytes (**Figure 4**), and estimates of the average density of expression of glutamate transporters (**Figure 1**, **Table 4**, **Table 5**), we can ask how much of the actual astrocytic membrane is occupied by transporters as opposed to other plasma membrane proteins. We distinguished the following

compartments: soma, stems (i.e. primary and secondary astrocyte branches), shafts and tips, for different values of insertion depth  $h_{in}$ . As explained before, we initially ignored potential restrictions due to crowding effects at branching points, and approximated the soma as a sphere and all branches as cylinders, with rounded tips at their endings. The maximum number of transporters that can be placed in a sphere of radius  $r_1$  is provided by Equation (17). Each one of the  $K$  primary branches of diameter  $\delta_1$  departing from the soma, however, covers a portion of the sphere surface that can be estimated as:

$$A_{cap} = 2\pi r_1 \left( r_1 - \sqrt{r_1^2 - (\delta_1/2)^2} \right)$$

This means that the effective fraction of the somatic surface where transporters can be expressed can be expressed as  $A_{soma} - K \cdot A_{cap}$ . The number of transporters in the soma can then be estimated as:

$$n_{soma} = \frac{A_{soma}}{4\pi r_1^2} \cdot n_{sphere} = \frac{4\pi r_1^2 - K \cdot A_{cap}}{4\pi r_1^2} \cdot n_{sphere} \quad (41)$$

where  $n_{sphere}(r_1)$  is given in Equation (26), and the area occupied by transporter trimers in the soma is:

$$S_{soma} = n_{soma} A_{sphere}^{\Delta}$$

Here, the area of the spherical portion replaced by the trimer  $A_{sphere}^{\Delta}(r_1)$  was provided by Equation (28). For the astrocyte branches, the total surface area  $A_{tree}$ , the number of transporter trimers  $n_{tree}$  and the total surface area occupied by the transporters  $S_{tree}$  were estimated based on the branching tree simulations as:

$$A_{tree} = \sum_{j=1}^B \frac{\pi \delta_j^2}{4} l_j \quad (42)$$

$$n_{tree} = \sum_{j=1}^B n_{cyl} \left( \frac{\delta_j}{2}, l_j \right) \quad (43)$$

$$S_{tree} = \sum_{j=1}^B n_{cyl} \left( \frac{\delta_j}{2}, l_j \right) A_{cyl}^{\Delta} \left( \frac{\delta_j}{2} \right) \quad (44)$$

where the sum sweeps all  $B$  branch segments  $1 \leq j \leq B$ , with lengths  $l_j$  and diameters  $\delta_j$  computed as specified in the Methods section (the average lengths for the first branching levels are shown in **Table 3** as the value of  $\lambda$  and the vector  $\chi$ ). Recall that the expression for  $A_{cyl}^{\Delta}(r_1)$  was provided by Equation (33). A combination of our formulas gave us the estimate for the total surface area of the astrocyte:

$$A_{total} = A_{soma} + A_{tree}$$

the number of transporter trimers:

$$n_{total} = n_{soma} + n_{tree}$$

and the fraction the astrocyte surface area occupied by the transporters:

$$S_{total} = S_{soma} + S_{tree}$$

We then calculated the surface transporter trimer density as:

$$\sigma = \frac{n_{total}}{A_{total}}$$

The surface density of glutamate transporter monomers was obtained by multiplying  $\sigma$  by three. The fraction of the astrocyte surface area occupied by the transporters was calculated as:

$$\Phi = \frac{S_{total}}{A_{total}}$$

We computed all these values from a set of model astrocytes generated using MATLAB simulations (n=10; **Figure 4B**). We compared their main geometric features of the model astrocytes with those of biocytin-filled astrocytes. These included: the volume of the neuropil occupied by the astrocyte, the cytoplasmic volume, as well as the branch length, number of branching points and branching levels (**Figure 4E**). In addition, we compared the 3D Sholl profiles (Figure 4F,G), branch length and branching angle (**Figure 4H,I**), to make sure that the model captured the main features of real astrocytes. We used this cohort of model astrocytes to calculate the surface area distribution of different sub-cellular compartments (**Figure 10A**). Although the tips are suggested to have the highest transporter density, these contribute only 0.2% of the entire astrocyte surface area. By contrast, the shafts represent  $\sim 68\%$  of the astrocyte area, and therefore represent the compartment most likely to be in the proximity of a synapse. In the same graph, we also show how the proportion of all GLAST and GLT-1 molecules varies between tips, stems, shafts and the soma (**Figure 10A**). Note that the soma area might appear small, due to the fact that we subtracted the cross-section area of primary branches from that of a sphere with the same radius as the astrocyte soma. The graphs show how the expression of GLAST is highest in the soma, whereas that of GLT-1 is highest in the tips. If transporters were the only molecules expressed on the astrocyte plasma membrane, crowding effects would pose an upper limit to their surface density in the tips and, to a lesser extent, in the shafts. These effects would become more pronounced as the transporters protrude towards the cytoplasm, as it happens when they are fully bound (**Figure 10B**) [62]. Consequently, the maximum surface density of glutamate transporters would be lowest in the tips, and progressively larger in the shafts, stems and soma, as the size of these sub-cellular compartments increases (**Figure 10C**). Varying the insertion depth of transporters at the tips can reduce their maximal surface density by  $\sim 10\%$ , and by  $\sim 5\%$  in the shafts, with a much smaller effect in the soma and shafts (**Figure 10C**). Clearly, whether these crowding effects take place or not, needs to take into account the actual values for the glutamate transporter relative surface density and occupancy. Therefore, we asked how much of the actual glutamate uptake capacity is used by astrocytes in different sub-cellular compartments and at different ages, assuming there is no major change in the surface area of these cells between 2-3 weeks and 15 month old mice (**Figure 10D**). In the tips, the relative transporter density varies from  $\sim 20\%$  to  $\sim 50\%$  between these two age groups. In the soma, this effect is less pronounced, as the age-dependent change goes from  $\sim 10\%$  to  $\sim 20\%$ . This means that only  $\sim 17\%$  of the surface area of the tips is occupied by glutamate transporters in 2-3 week old mice, whereas this proportion increases to  $\sim 40\%$  in 15 month old mice assuming there are major changes in surface area (**Figure 10E**). Together, these findings indicate that although crowding effects can in principle limit the local expression of membrane proteins like astrocytes, whether this happens or not, depends on the expression of all other proteins on the cell membrane of a given sub-cellular compartment.

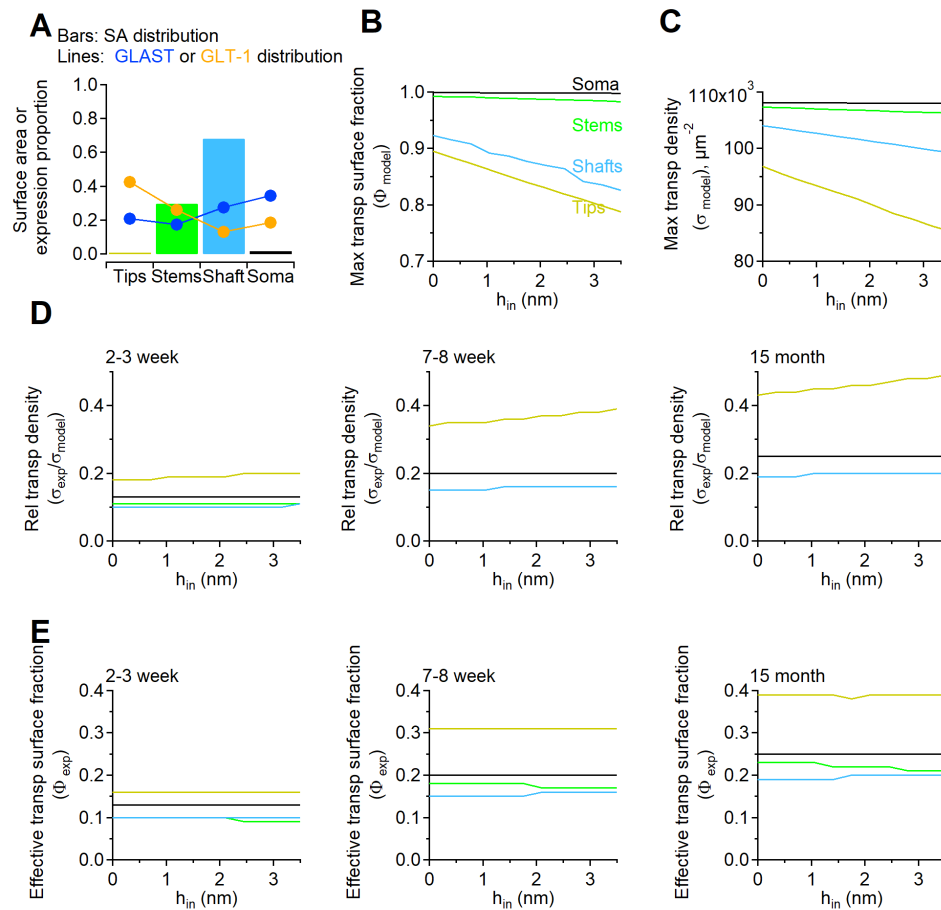


**Figure 10: Glutamate transporter distribution in different astrocyte sub-cellular compartments.** **A.** The color-coded bar graphs represent the surface area distribution in four different astrocyte sub-cellular compartments. The tips represent the hemispheric ending of the terminal branches. The stems represent the sum of primary and secondary branches. The soma represents the surface area of a spherical representation of the soma minus the surface area of the sphere underlying the base of the primary branches. The shafts represent all other compartments that are not part of those described above. The blue line and filled circles described the relative distribution of GLAST in different sub-cellular compartments [59, 60]. Analogous measures for the distribution of GLT-1 are shown using the orange line and filled circles. For both GLAST and GLT-1 we scaled these proportions from [59, 60] so that their sum was 1. **B.** Measures of the ratio between the maximal surface area of the model cell that can be occupied by transporters in each compartment, divided by the actual surface area of the same compartment. **C.** Maximal transporter surface density that can be achieved in each sub-cellular domain. **D.** Relative transporter surface density, measured as the ratio between the experimentally measured transporter density, distributed in each compartment (**Table 6**), and analogous measures obtained from the model shown in C, for 2-3 week (*left*), 7-8 week (*middle*), and 15 month old mice (*right*). **E.** Effective fraction of the maximal astrocyte surface area occupied by transporters in each compartment, in the same age groups described in D. In these graphs, the values of  $\phi_{exp}$  were calculated as  $\phi_{exp} = \sigma_{exp}/\sigma_{model} \cdot \phi_{model}$ .

## Discussion

### Comparison of present and past findings

Currently available estimates of glutamate transporter density have been widely used in modeling studies of glutamate diffusion, uptake and cross-talk among synapses [23, 24, 29, 30, 33, 40, 48, 66–69].



These estimates, obtained from 7–8 week old rats, showed that the total concentration of glutamate transporters in the hippocampus *stratum radiatum* is  $\sim 30 \mu\text{M}$  [28]. As mice have become widely used in the scientific community, it is important to determine whether these estimates provide a good approximation of the glutamate transporter concentration and surface density in astrocytes of the mouse hippocampus. Our results show that the concentration of these transporter is higher in mice compared to rats, and varies between  $70 \mu\text{M}$  in 2-3 week old mice to  $151 \mu\text{M}$  in 15 month old mice. Since the extracellular space in the mouse hippocampus is  $\sim 15\%$  [29], the effective concentration of glutamate transporters in portions of the extracellular space delimited by astrocytic membranes is likely in the order of  $0.49 - 1 \text{ mM}$  (cf.  $0.14-0.33$  in rats). This difference is partly due to the higher density of astrocyte membranes in the mouse neuropil:  $3.15 \mu\text{m}^2/\mu\text{m}^3$  in mice compared to  $1.4 \mu\text{m}^2/\mu\text{m}^3$  in rats [53,54]. Assuming that the total plasma membrane density is  $14 \mu\text{m}^2/\mu\text{m}^3$  [28], then the fraction of the extracellular space enclosed between an astrocyte membrane and any other membrane is 18% in rats and 34% in mice (i.e.  $2 \cdot 1.4/14 \cdot (14 - 1.4)/14$  and  $2 \cdot 3.15/14 \cdot (14 - 3.15)/14 \mu\text{m}^2/\mu\text{m}^3$ , respectively). This means that in the mouse hippocampus, the effective concentration of glutamate transporters in portions of the extracellular space flanked by astrocytic and non-astrocytic membranes is  $1.4 - 3 \text{ mM}$ , depending on the mouse age. These values are significantly higher than those previously reported in mice, and suggest that the glutamate uptake capacity in the hippocampus can vary substantially among rodents. This information adds to known differences in the transcriptomics landscape of astrocytes of different species, including mouse and humans [70]. Within the same species, glutamate uptake also varies among different brain regions and changes with neuronal activity [71–74]. Whether these regional differences and susceptibility to modulation are evolutionarily conserved or vary across species remains to be determined.

## Age-dependent changes in glutamate transporter expression

A natural decline in the expression of astrocytic glutamate transporters has been suggested to occur in humans (8 – 40 versus and 40 – 63 years old) [70] and rats (3 – 6 month versus 24 – 27 month old) [75], (3 month versus 24 month old) [76]. A decline in glutamate transporter expression has also been detected in neurodegenerative disease like attention deficit hyperactivity disorder [77,78], autism [77,79], depression [80–82] and Alzheimer’s disease [83–86], prompting the idea that it may represent an important risk factor for these disease [87]. Our data are not in conflict with these findings, as they speak for an age range that precedes the one studied by these other works, and that coincides with adolescence (2-3 weeks), young adulthood (7-8 weeks) and middle age (15 months). Within the age window analyzed in our work, the expression of glutamate transporters does not decline, but rather increases. Together, these findings indicate that the expression of the astrocyte glutamate transporters GLAST and GLT-1 increases progressively from adolescence to middle, before declining with aging. This increased expression could function to preserve the spatial specificity of synaptic transmission, limiting the ability of glutamate to activate receptors at a distance from its release site. It could also provide a mechanism to reduce further the steady-state concentration of glutamate in the extracellular space, with potentially notable effects on fast synaptic transmission, short- and long-term plasticity, as well as on the dynamics of biosynthetic mechanisms to regulate glutamate biosynthesis and degradation in astrocytes.

## Uneven distribution of glutamate transporters along the plasma membrane of astrocytes

Glutamate transporters are unevenly distributed along the astrocytic plasma membrane [53,56,57]. Accordingly, immunostaining experiments in hippocampal sections and organotypic slice cultures show that GLT-1 forms small clusters in lamellae and filopodia-like processes, the size and distribution of which can be modulated by neuronal activity [56]. This confined expression, which is a

common property among transporters with trimeric assembly like ASCT1, is not attributed to the presence of consensus sequences in the cytoplasmic tails of the transporters, which act as binding sites of cytosolic scaffolding proteins. Instead, it has been suggested to be due to the presence of an extracellular loop at the center of the 4<sup>th</sup> transmembrane helices, not far from the glutamate binding sites, which does not require transporter activity [59]. In the astrocyte tips, at the end of astrocyte branches, the surface density of glutamate transporters is high, due to the presence of a transmembrane domain acting as a sorting signal to the astrocyte processes tips [59]. The increased density of glutamate transporter in astrocytes tips is largely due to a 2.3-fold increase in GLT-1 expression in the tips compared to the soma [59,60]. By contrast, GLAST is 0.6-fold less abundant in the tips compared to the soma. These findings indicate that the molecular mechanisms responsible for sorting glutamate transporters to different sub-cellular compartments might differ among specific variants [59,60]. Our data show that these tips, defined as the hemispheric cap of a terminal process, represent a very small portion of the surface area of an astrocyte ( $0.28 \pm 0.03\%$ ). A typical astrocyte occupies a  $588,000 \mu m^3$  domain of the hippocampus (**Figure 4E**). Within this volume, there are  $588,000 - 1,764,000$  synapses, based on anatomical estimates suggesting that there are  $1 - 3 \mu m^{-3}$  synapses in the hippocampal neuropil [88]. Given that only 57% of these synapses have an astrocytic process apposed to them [4], the number of synapses contacted by an astrocyte is  $335,000 - 1,005,000$ . This number is higher than the average number of tips of an astrocyte (2,200): only 0.2 – 0.6% of all synapses in the neuropil volume occupied by an astrocyte are contacted by a tip. For GLAST, the the tip:shaft:stem:soma expression ratio with respect to the soma is 0.6:0.5:0.8:1, whereas this is 2.3:1.4:0.7:1 for GLT-1. In other words, the tip:shaft:stem:soma expression ratio with respect to the soma of all glutamate transporters is 1.4:0.9:0.7:1. This means that  $> 99\%$  synapses have only 50 – 71% of the glutamate transporters found at synapses contacted by astrocyte tips. Since changes in the local density of glutamate transporters alter the extent of extrasynaptic AMPA/NMDA receptor activation, these findings indicate that there is a significant proportion of synapses where the activation of these receptors is favored. Our findings also indicate that crowding effects may introduce an upper limit to the expression of glutamate transporters in spatially confined astrocytic processes. This, in turn, could contribute to the limited surface mobility of these molecules in astrocyte tips [2].

### The 3/2 rule applies to astrocytes

According to Rall's equivalent cylinder model, the complexity of branching geometries of cells can be reduced to that of a simple cylinder [45]. This condition is satisfied, in neurons, when the relationship between the diameter of the parent and daughter branches at a particular branching point follows a constraint commonly referred to as the 3/2 rule [45–47]. Under these conditions, the input conductance of dendritic branches depends on the 3/2 power of the branch diameter [45]. Our anatomical measures indicate that the diameter distribution of daughter and parent astrocytic branches at a branching point can also be described by the 3/2 rule (**Table 3**). The ability to map the entire branching geometry of an astrocyte as an equivalent cylinder according to the 3/2 rule means that the input conductance of each branch cylinder also depends on the 3/2 power of its diameter and that the fundamental rules of passive signal propagation and integration through astrocyte branches share the same biophysical properties of neurons, validating the use of compartmental models for these cells.

### Conclusions

Together, our findings provide a quantitative framework to study signal propagation in astrocytes, and estimates of glutamate transporter expression in the mouse hippocampus at different ages. Strikingly, the identity of the sub-cellular domain of the astrocyte membrane that is in contact with

a synapse is a major determinant of glutamate spillover and extrasynaptic receptor activation, due to the uneven distribution of glutamate transporters.

# References

- [1] Niels C Danbolt. Glutamate uptake. *Progress in Neurobiology*, 65(1):1–105, 2001.
- [2] Ciaran Murphy-Royal, Julien P Dupuis, Juan A Varela, Aude Panatier, Benoît Pinson, Jérôme Baulieu, Laurent Groc, and Stéphane HR Olié. Surface diffusion of astrocytic glutamate transporters shapes synaptic transmission. *Nature Neuroscience*, 18(2):219–226, 2015.
- [3] Piotr Michaluk, Janosch Peter Heller, and Dmitri A Rusakov. Rapid recycling of glutamate transporters on the astroglial surface. *Elife*, 10:e64714, 2021.
- [4] Rachel Ventura and Kristen M Harris. Three-dimensional relationships between hippocampal synapses and astrocytes. *The Journal of Neuroscience*, 19(16):6897–6906, 1999.
- [5] Noa Zerangue and Michael P Kavanaugh. Flux coupling in a neuronal glutamate transporter. *Nature*, 383(6601):634, 1996.
- [6] Jacques I Wadiche, Jeffrey L Arriza, Susan G Amara, and Michael P Kavanaugh. Kinetics of a human glutamate transporter. *Neuron*, 14(5):1019–1027, 1995.
- [7] Jacques I Wadiche and Michael P Kavanaugh. Macroscopic and microscopic properties of a cloned glutamate transporter/chloride channel. *The Journal of Neuroscience*, 18(19):7650–7661, 1998.
- [8] Wendy A Fairman, Robert J Vandenberg, Jeffrey L Arriza, Michael P Kavanaugh, and Susan G Amara. An excitatory amino-acid transporter with properties of a ligand-gated chloride channel. *Nature*, 375(6532):599–603, 1995.
- [9] Jeffrey L Arriza, Scott Eliasof, Michael P Kavanaugh, and Susan G Amara. Excitatory Amino Acid Transporter 5, a retinal glutamate transporter coupled to a chloride conductance. *Proceedings of the National Academy of Sciences*, 94(8):4155–4160, 1997.
- [10] Jacques I Wadiche, Susan G Amara, and Michael P Kavanaugh. Ion fluxes associated with excitatory amino acid transport. *Neuron*, 15(3):721–728, 1995.
- [11] Margaret L Veruki, Svein H Mørkve, and Espen Hartveit. Activation of a presynaptic glutamate transporter regulates synaptic transmission through electrical signaling. *Nature Neuroscience*, 9(11):1388–1396, 2006.
- [12] Jeffrey L Arriza, Wendy A Fairman, Jacques I Wadiche, Geoffrey H Murdoch, Michael P Kavanaugh, and Susan G Amara. Functional comparisons of three glutamate transporter subtypes cloned from human motor cortex. *The Journal of Neuroscience*, 14(9):5559–5569, 1994.
- [13] Takashi Shibata, Masahiko Watanabe, Kohichi Tanaka, Keiji Wada, and Yoshiro Inoue. Dynamic changes in expression of glutamate transporter mRNAs in developing brain. *Neuroreport*, 7(3):705–709, 1996.
- [14] Anastassios V Tzingounis and Jacques I Wadiche. Glutamate transporters: confining runaway excitation by shaping synaptic transmission. *Nature Reviews Neuroscience*, 8(12):935–947, 2007.
- [15] Renae M Ryan, Susan L Ingram, and Annalisa Scimemi. Regulation of glutamate, gaba and dopamine transporter uptake, surface mobility and expression. *Frontiers in Cellular Neuroscience*, 2021.

- [16] Dinesh Yernool, Olga Boudker, Yan Jin, and Eric Gouaux. Structure of a glutamate transporter homologue from *Pyrococcus horikoshii*. *Nature*, 431(7010):811, 2004.
- [17] Nicolas Reyes, Christopher Ginter, and Olga Boudker. Transport mechanism of a bacterial homologue of glutamate transporters. *Nature*, 462(7275):880, 2009.
- [18] Ichia Chen, Shashank Pant, Qianyi Wu, Rosemary J Cater, Meghna Sobti, Robert J Vandenberg, Alastair G Stewart, Emad Tajkhorshid, Josep Font, and Renae M Ryan. Glutamate transporters have a chloride channel with two hydrophobic gates. *Nature*, 591(7849):327–331, 2021.
- [19] C Alleva, Kirill Kovalev, R Astashkin, MI Berndt, C Baeken, T Balandin, Valentin Gordeliy, Ch Fahlke, and J-P Machtens. Na<sup>+</sup>-dependent gate dynamics and electrostatic attraction ensure substrate coupling in glutamate transporters. *Science advances*, 6(47):eaba9854, 2020.
- [20] Grégory Verdon and Olga Boudker. Crystal structure of an asymmetric trimer of a bacterial glutamate transporter homolog. *Nature Structural & Molecular Biology*, 19(3):355, 2012.
- [21] Greg P Leary, David C Holley, Emily F Stone, Brent R Lyda, Leonid V Kalachev, and Michael P Kavanaugh. The central cavity in trimeric glutamate transporters restricts ligand diffusion. *Proceedings of the National Academy of Sciences*, 108(36):14980–14985, 2011.
- [22] Dmitri A Rusakov and Dimitri M Kullmann. Extrasynaptic glutamate diffusion in the hippocampus: ultrastructural constraints, uptake, and receptor activation. *The Journal of Neuroscience*, 18(9):3158–3170, 1998.
- [23] Jeffrey S Diamond. Deriving the glutamate clearance time course from transporter currents in CA1 hippocampal astrocytes: transmitter uptake gets faster during development. *The Journal of Neuroscience*, 25(11):2906–2916, 2005.
- [24] Boris Barbour. An evaluation of synapse independence. *The Journal of Neuroscience*, 21(20):7969–7984, 2001.
- [25] Michiko Takahashi, Monique Sarantis, and David Attwell. Postsynaptic glutamate uptake in rat cerebellar Purkinje cells. *The Journal of Physiology*, 497(2):523–530, 1996.
- [26] Dwight E Bergles and Craig E Jahr. Synaptic activation of glutamate transporters in hippocampal astrocytes. *Neuron*, 19(6):1297–1308, 1997.
- [27] Thomas S Otis, Michael P Kavanaugh, and Craig E Jahr. Postsynaptic glutamate transport at the climbing fiber-Purkinje cell synapse. *Science*, 277(5331):1515–1518, 1997.
- [28] Knut P Lehre and Niels C Danbolt. The number of glutamate transporter subtype molecules at glutamatergic synapses: chemical and stereological quantification in young adult rat brain. *The Journal of Neuroscience*, 18(21):8751–8757, 1998.
- [29] Annalisa Scimemi, Hua Tian, and Jeffrey S Diamond. Neuronal transporters regulate glutamate clearance, NMDA receptor activation, and synaptic plasticity in the hippocampus. *The Journal of Neuroscience*, 29(46):14581–14595, 2009.
- [30] Knut P Lehre and Dmitri A Rusakov. Asymmetry of glia near central synapses favors presynaptically directed glutamate escape. *Biophysical Journal*, 83(1):125–134, 2002.
- [31] Leonid P Savtchenko and Dmitri A Rusakov. Extracellular diffusivity determines contribution of high-versus low-affinity receptors to neural signaling. *Neuroimage*, 25(1):101–111, 2005.

- [32] Dmitri A Rusakov. The role of perisynaptic glial sheaths in glutamate spillover and extracellular  $\text{Ca}^{2+}$  depletion. *Biophysical Journal*, 81(4):1947–1959, 2001.
- [33] Kevin M Franks, Thomas M Bartol, and Terrence J Sejnowski. A Monte Carlo model reveals independent signaling at central glutamatergic synapses. *Biophysical Journal*, 83(5):2333–2348, 2002.
- [34] Kevin M Franks, Charles F Stevens, and Terrence J Sejnowski. Independent sources of quantal variability at single glutamatergic synapses. *The Journal of Neuroscience*, 23(8):3186–3195, 2003.
- [35] Jeffrey S Diamond. Neuronal glutamate transporters limit activation of NMDA receptors by neurotransmitter spillover on CA1 pyramidal cells. *The Journal of Neuroscience*, 21(21):8328–8338, 2001.
- [36] Kaiyu Zheng, Annalisa Scimemi, and Dmitri A Rusakov. Receptor actions of synaptically released glutamate: the role of transporters on the scale from nanometers to microns. *Biophysical Journal*, 95(10):4584–4596, 2008.
- [37] Martin F Hohmann-Marriott, Alioscka A Sousa, Afrouz A Azari, Svetlana Glushakova, Guofeng Zhang, Joshua Zimmerberg, and Richard D Leapman. Nanoscale 3D cellular imaging by axial scanning transmission electron tomography. *Nature Methods*, 6(10):729–731, 2009.
- [38] Alioscka A Sousa, Afrouz A Azari, Guofeng Zhang, and Richard D Leapman. Dual-axis electron tomography of biological specimens: Extending the limits of specimen thickness with bright-field stem imaging. *The Journal of Structural Biology*, 174(1):107–114, 2011.
- [39] Paul W Tillberg, Fei Chen, Kiryl D Piatkevich, Yongxin Zhao, Chih-Chieh Jay Yu, Brian P English, Linyi Gao, Anthony Martorell, Ho-Jun Suk, Fumiaki Yoshida, et al. Protein-retention expansion microscopy of cells and tissues labeled using standard fluorescent proteins and antibodies. *Nature Biotechnology*, 34(9):987–992, 2016.
- [40] John P McCauley, Maurice A Petroccione, Lianna Y D’Brant, Gabrielle C Todd, Nurat Affinnih, Justin J Wisnoski, Shergil Zahid, Swasti Shree, Alioscka A Sousa, Rose M De Guzman, et al. Circadian modulation of neurons and astrocytes controls synaptic plasticity in hippocampal area CA1. *Cell Reports*, 33(2):108255, 2020.
- [41] William E Lorensen and Harvey E Cline. Marching cubes: A high resolution 3D surface construction algorithm. *ACM Siggraph Computer Graphics*, 21(4):163–169, 1987.
- [42] Thomas A Nielsen, David A DiGregorio, and R Angus Silver. Modulation of glutamate mobility reveals the mechanism underlying slow-rising amper epcscs and the diffusion coefficient in the synaptic cleft. *Neuron*, 42(5):757–771, 2004.
- [43] Peter Jonas, Guy Major, and Bert Sakmann. Quantal components of unitary epcscs at the mossy fibre synapse on CA3 pyramidal cells of rat hippocampus. *The Journal of Physiology*, 472(1):615–663, 1993.
- [44] Robin A Lester and Craig E Jahr. NMDA channel behavior depends on agonist affinity. *The Journal of Neuroscience*, 12(2):635–643, 1992.
- [45] Wilfrid Rall. Branching dendritic trees and motoneuron membrane resistivity. *Experimental Neurology*, 1(5):491–527, 1959.



- [46] Wilfrid Rall and John Rinzel. Branch input resistance and steady attenuation for input to one branch of a dendritic neuron model. *Biophysical Journal*, 13(7):648–688, 1973.
- [47] John Rinzel and Wilfrid Rall. Transient response in a dendritic neuron model for current injected at one branch. *Biophysical Journal*, 14(10):759, 1974.
- [48] Amanda M Sweeney, Kelsey E Fleming, John P McCauley, Marvin F Rodriguez, Elliot T Martin, Alioscka A Sousa, Richard D Leapman, and Annalisa Scimemi. PAR1 activation induces rapid changes in glutamate uptake and astrocyte morphology. *Scientific Reports*, 7:43606, 2017.
- [49] Oliver H Lowry, Nira R Roberts, Katherine Y Leiner, Mei-Ling Wu, A Lewis Farr, and R Wayne Albers. The quantitative histochemistry of brain III. Ammon’s horn. *The Journal of Biological Chemistry*, 207(1):39–50, 1954.
- [50] Oliver H Lowry. The quantitative histochemistry of the brain: Histological sampling. *The Journal of Histochemistry & Cytochemistry*, 1(6):420–428, 1953.
- [51] Thorsten Storck, Stefan Schulte, Kay Hofmann, and Wilhelm Stoffel. Structure, expression, and functional analysis of a  $\text{Na}^+$ -dependent glutamate/aspartate transporter from rat brain. *Proceedings of the National Academy of Sciences*, 89(22):10955–10959, 1992.
- [52] Gilia Pines, Niels C Danbolt, Magnar Bjørås, Yumin Zhang, Annie Bendahan, Lars Eide, Hermann Koepsell, Jon Storm-Mathisen, Erling Seeberg, and Baruch I Kanner. Cloning and expression of a rat brain L-glutamate transporter. *Nature*, 360(6403):464–467, 1992.
- [53] Farrukh A Chaudhry, Knut P Lehre, Menno van Lookeren Campagne, Ole P Ottersen, Niels C Danbolt, and Jon Storm-Mathisen. Glutamate transporters in glial plasma membranes: highly differentiated localizations revealed by quantitative ultrastructural immunocytochemistry. *Neuron*, 15(3):711–720, 1995.
- [54] Knut P Lehre, Line M Levy, Ole P Ottersen, Jon Storm-Mathisen, and Niels C Danbolt. Differential expression of two glial glutamate transporters in the rat brain: quantitative and immunocytochemical observations. *The Journal of Neuroscience*, 15(3):1835–1853, 1995.
- [55] Thomas Schikorski and Charles F Stevens. Quantitative ultrastructural analysis of hippocampal excitatory synapses. *The Journal of Neuroscience*, 17(15):5858–5867, 1997.
- [56] Adrienne M Benediktsson, Glen S Marrs, Jian Cheng Tu, Paul F Worley, Jeffrey D Rothstein, Dwight E Bergles, and Michael E Dailey. Neuronal activity regulates glutamate transporter dynamics in developing astrocytes. *Glia*, 60(2):175–188, 2012.
- [57] NC Danbolt, J Storm-Mathisen, and BI Kanner. A  $\text{Na}^+/\text{K}^+$  coupled-glutamate transporter purified from rat brain is located in glial cell processes. *Neuroscience*, 51(2):295–310, 1992.
- [58] Jeffrey D Rothstein, Lee Martin, Allan I Levey, Margaret Dykes-Hoberg, Lin Jin, David Wu, Norman Nash, and Ralph W Kuncl. Localization of neuronal and glial glutamate transporters. *Neuron*, 13(3):713–725, 1994.
- [59] Mariko Kato Hayashi and Masato Yasui. The transmembrane transporter domain of glutamate transporters is a process tip localizer. *Scientific Reports*, 5(1):1–8, 2015.
- [60] Andreas Reichenbach, Amin Derouiche, and Frank Kirchhoff. Morphology and dynamics of perisynaptic glia. *Brain Research Reviews*, 63(1-2):11–25, 2010.

- [61] Gerrit Van Meer, Dennis R Voelker, and Gerald W Feigenson. Membrane lipids: where they are and how they behave. *Nature Reviews Molecular Cell Biology*, 9(2):112, 2008.
- [62] Olga Boudker, Renae M Ryan, Dinesh Yernool, Keiko Shimamoto, and Eric Gouaux. Coupling substrate and ion binding to extracellular gate of a sodium-dependent aspartate transporter. *Nature*, 445(7126):387, 2007.
- [63] Nurunisa Akyuz, Roger B Altman, Scott C Blanchard, and Olga Boudker. Transport dynamics in a glutamate transporter homologue. *Nature*, 502(7469):114, 2013.
- [64] Maarten Groeneveld and Dirk-Jan Slotboom.  $\text{Na}^+$ :aspartate coupling stoichiometry in the glutamate transporter homologue Glt<sub>Ph</sub>. *Biochemistry*, 49(17):3511–3513, 2010.
- [65] Grégory Verdon, SeCheol Oh, Ryan N Serio, and Olga Boudker. Coupled ion binding and structural transitions along the transport cycle of glutamate transporters. *eLife*, 3, 2014.
- [66] Christian Henneberger, Lucie Bard, Aude Panatier, James P Reynolds, Olga Kopach, Nikolay I Medvedev, Daniel Minge, Michel K Herde, Stefanie Anders, Igor Kraev, et al. Ltp induction boosts glutamate spillover by driving withdrawal of perisynaptic astroglia. *Neuron*, 108(5):919–936, 2020.
- [67] Moritz Armbruster, Chris G Dulla, and Jeffrey S Diamond. Effects of fluorescent glutamate indicators on neurotransmitter diffusion and uptake. *eLife*, 9:e54441, 2020.
- [68] Leonid P Savtchenko, Lucie Bard, Thomas P Jensen, James P Reynolds, Igor Kraev, Nikolay Medvedev, Michael G Stewart, Christian Henneberger, and Dmitri A Rusakov. Disentangling astroglial physiology with a realistic cell model in silico. *Nature Communications*, 9(1):1–15, 2018.
- [69] Nikolay Gavrilov, Inna Golyagina, Alexey Brazhe, Annalisa Scimemi, Vadim Turlapov, and Alexey Semyanov. Astrocytic coverage of dendritic spines, dendritic shafts, and axonal boutons in hippocampal neuropil. *Frontiers in Cellular Neuroscience*, 12:248, 2018.
- [70] Ye Zhang, Steven A Sloan, Laura E Clarke, Christine Caneda, Colton A Plaza, Paul D Blumenthal, Hannes Vogel, Gary K Steinberg, Michael SB Edwards, Gordon Li, et al. Purification and characterization of progenitor and mature human astrocytes reveals transcriptional and functional differences with mouse. *Neuron*, 89(1):37–53, 2016.
- [71] Jennifer Romanos, Dietmar Benke, Aiman S Saab, Hanns Ulrich Zeilhofer, and Mirko Santello. Differences in glutamate uptake between cortical regions impact neuronal nmda receptor activation. *Communications biology*, 2(1):1–15, 2019.
- [72] Giselle Cheung, Jérémie Sibille, Jonathan Zapata, and Nathalie Rouach. Activity-dependent plasticity of astroglial potassium and glutamate clearance. *Neural plasticity*, 2015.
- [73] Moritz Armbruster, Elizabeth Hanson, and Chris G Dulla. Glutamate clearance is locally modulated by presynaptic neuronal activity in the cerebral cortex. *Journal of Neuroscience*, 36(40):10404–10415, 2016.
- [74] Nawrin Ferdous Pinky. *Region-and activity-dependent regulation of extracellular glutamate in the brain*. PhD thesis, Memorial University of Newfoundland, 2018.
- [75] Brigitte Potier, Jean-Marie Billard, Sylvain Riviere, Pierre-Marie Sinet, Isabelle Denis, Gaelle Champeil-Potokar, Barbara Grntal, Anne Jouvenceau, Melanie Kollen, and Patrick Dutar.

- Reduction in glutamate uptake is associated with extrasynaptic nmda and metabotropic glutamate receptor activation at the hippocampal ca1 synapse of aged rats. *Aging Cell*, 9(5):722–735, 2010.
- [76] Holly M Brothers, Isabelle Bardou, Sarah C Hopp, Roxanne M Kaercher, Angela W Corona, Ashley M Fenn, Jonathan P Godbout, and Gary L Wenk. Riluzole partially rescues age-associated, but not lps-induced, loss of glutamate transporters and spatial memory. *Journal of neuroimmune pharmacology*, 8(5):1098–1105, 2013.
  - [77] Claudia JM van Amen-Hellebrekers, Sandra Jansen, Rolph Pfundt, Janneke H Schuurs-Hoeijmakers, David A Koolen, Carlo L Marcelis, Nicole de Leeuw, and Bert BA de Vries. Duplications of *slc1a3*: Associated with adhd and autism. *European journal of medical genetics*, 59(8):373–376, 2016.
  - [78] Xin Huang, Qi Zhang, Xinzhen Chen, Xue Gu, Min Wang, and Jing Wu. A functional variant in *slc1a3* influences adhd risk by disrupting a hsa-mir-3171 binding site: A two-stage association study. *Genes, Brain and Behavior*, 18(5):e12574, 2019.
  - [79] Haruki Higashimori, Christina S Schin, Ming Sum R Chiang, Lydie Morel, Temitope A Shon-eye, David L Nelson, and Yongjie Yang. Selective deletion of astroglial *fmrp* dysregulates glutamate transporter *glt1* and contributes to fragile x syndrome phenotypes in vivo. *Journal of Neuroscience*, 36(27):7079–7094, 2016.
  - [80] Caren J Blacker, Vincent Millischer, Lauren M Webb, Ada MC Ho, Martin Schalling, Mark A Frye, and Marin Veldic. *Eaat2* as a research target in bipolar disorder and unipolar depression: a systematic review. *Molecular neuropsychiatry*, 5(1):44–59, 2019.
  - [81] René Bernard, Ilan A Kerman, Robert C Thompson, Edward G Jones, William E Bunney, Jack D Barchas, Alan F Schatzberg, Richard M Myers, Huda Akil, and Stanley J Watson. Altered expression of glutamate signaling, growth factor, and glia genes in the locus coeruleus of patients with major depression. *Molecular psychiatry*, 16(6):634–646, 2011.
  - [82] Prabhakara V Choudary, M Molnar, SJ Evans, H Tomita, JZ Li, MP Vawter, RM Myers, WE Bunney, H Akil, SJ Watson, et al. Altered cortical glutamatergic and gabaergic signal transmission with glial involvement in depression. *Proceedings of the National Academy of Sciences*, 102(43):15653–15658, 2005.
  - [83] Annalisa Scimemi, James S Meabon, Randall L Woltjer, Jane M Sullivan, Jeffrey S Diamond, and David G Cook. Amyloid- $\beta$ 1–42 slows clearance of synaptically released glutamate by mislocalizing astrocytic *glt-1*. *Journal of Neuroscience*, 33(12):5312–5318, 2013.
  - [84] Paramita Mookherjee, Pattie S Green, G Watson, Marcos A Marques, Kohichi Tanaka, Kole D Meeker, James S Meabon, Ning Li, Ping Zhu, Valerie G Olson, et al. *Glt-1* loss accelerates cognitive deficit onset in an alzheimer’s disease animal model. *Journal of Alzheimer’s disease*, 26(3):447–455, 2011.
  - [85] Kole D Meeker, James S Meabon, and David G Cook. Partial loss of the glutamate transporter *glt-1* alters brain akt and insulin signaling in a mouse model of alzheimer’s disease. *Journal of Alzheimer’s Disease*, 45(2):509–520, 2015.
  - [86] Ana C Pereira, Jason D Gray, Joshua F Kogan, Rina L Davidson, Todd G Rubin, Masahiro Okamoto, John H Morrison, and Bruce S McEwen. Age and alzheimer’s disease gene expression profiles reversed by the glutamate modulator riluzole. *Molecular psychiatry*, 22(2):296–305, 2017.

- [87] Alison C Todd and Giles E Hardingham. The regulation of astrocytic glutamate transporters in health and neurodegenerative diseases. *International journal of molecular sciences*, 21(24):9607, 2020.
- [88] Karin E Sorra, John C Fiala, and Kristen M Harris. Critical assessment of the involvement of perforations, spinules, and spine branching in hippocampal synapse formation. *Journal of Comparative Neurology*, 398(2):225–240, 1998.